Supplementary Information

Electrochemically-Induced Partial Cation Disorder Eliminates Lattice Collapse in Compositionally-Simple $LiNi_{0.9}Mn_{0.1}O_2$

Junghwa Lee[a,†], **Zhelong Jiang**[a,b,c,†,*], **Nicolas B. Liang**[a], **Howie Nguyen**[d,e], **Grace M. Busse**[a], **Jin Hwan Kwak**[f], **Yiseul Yoo**[f], **Hari Ramachandran**[a], **Kipil Lim**[a,b,c,g], **Peter M. Csernica**[a], **Tianyi Li**[h], **Xin Xu**[a,g], **Kyung Yoon Chung**[f], **Kathrin Michel**[i], **Joop Frerichs**[i], **William E. Gent**[a], **Raphaële J. Clément**[d,e], **Jungjin Park**[f,*], and **William C. Chueh**[a,b,g,*]

[a]Department of Materials Science and Engineering, Stanford University, Stanford, CA 94305, USA; [b]Applied Energy Division, SLAC National Accelerator Laboratory, Menlo Park, CA 94025, USA; [c]Stanford Synchrotron Radiation Lightsource, SLAC National Accelerator Laboratory, Menlo Park, CA 94025, USA; [d]Materials Department, University of California Santa Barbara, Santa Barbara, CA 93106, USA; [e]Materials Research Laboratory, University of California Santa Barbara, Santa Barbara, CA 93106, USA; [f]Energy Storage Research Center, Korea Institute of Science and Technology (KIST), Seoul 02792, Republic of Korea; [g]Stanford Institute for Materials and Energy Sciences, SLAC National Accelerator Laboratory, Menlo Park, CA 94025, USA; [h]X-ray Science Division, Argonne National Laboratory, Lemont, IL 60439, USA; [i]Battery Materials and Recycling, BASF SE, Ludwigshafen 67056, Germany; [z]Present address: The Polytechnic School, Ira. A. Fulton Schools of Engineering, Arizona State University, Mesa, AZ 85212, USA

[†] Junghwa Lee and Zhelong Jiang contributed equally to this work.

[*] Corresponding authors.
E-mail: wchueh@stanford.com; jpark716@kist.re.kr; zjiang18@slac.stanford.edu

Contents

1. Materials and Methods

1.1. Materials and Syntheses.

All boron-coated lithium nickel manganese oxides samples were made using the method of co-precipitation followed by solid-state synthesis.

First, co-precipitation was used to produce hydroxide precursor $Ni_{0.9}Mn_{0.1}(OH)_2$. A 1.5 M aqueous solution of $NiSO_4 \cdot 6H_2O$ and $MnSO_4 \cdot H_2O$ was prepared with 9:1 molar ratio of Ni:Mn. The mixed solution was pumped into a batch-type reactor under argon atmosphere to remove dissolved oxygen in deionized (DI) water, preventing undesirable manganese oxidation. At the same time, 4.0 M NaOH and 14.8 M $NH_3 \cdot H_2O$ precipitating solutions were prepared and added to regulate the pH and complexing agent concentrations. The reactor's pH was consistently maintained at 11.8 by the continuous inflow of NaOH solution during the co-precipitation progress. The process was conducted at 50 °C, facilitated by a hot water circulation system, with stirring for 20 h. The precipitates were vacuum filtered, washed with distilled water to remove the residual sodium ions, and then dried overnight at 80 °C in an oven.

Second, solid-state reactions were carried out between the mixture of $Ni_{0.9}Mn_{0.1}(OH)_2$, $LiOH \cdot H_2O$ (Honeywell Research Chemicals), and $B(OH)_3$ (Sigma-Aldrich). Boron is known to segregate and form a borate glass (a fast Li-ion conductor) coating on the particle surface, facilitating interfacial ionic transport and protects against surface degradation[23–26] without affecting the bulk properties. To make samples LNR0, LNR3, LNR5, LNR7, and LNR9 having electrochemically-active phases with compositions of $Li_{1+i}(Ni_{0.9}Mn_{0.1})_{1\text{-}i}O_2$ with $i = 0.00$, 0.03, 0.05, 0.07, and 0.09 (see Supplementary Information section 3 on how compositions were determined), reactant mixtures with nominal B:Li:(Ni+Mn) mol ratios of 0.01:1.01:1.00, 0.01:1.07:0.94, 0.01:1.10:0.91, 0.01:1.13:0.88, and 0.01:1.16:0.85 were used respectively (Supplementary Fig. 1). The reactant mixture was homogenized in a tube mill (IKA) before transferred to a tube furnace for calcination. Calcination was performed under continuous oxygen flow (1.4 L/min), with 10 h hold at 500 °C, followed by 15 h hold at maximum temperature (with 3 °C/min heating rate and furnace cooling). The optimized maximum temperature was 730, 700, 685, 670, and 650 °C for LNR0, LNR3, LNR5, LNR7, and LNR9 respectively. The materials synthesized contained secondary particles about 9 µm in diameter, which consist of elongated primary particles (Supplementary Fig. 2).

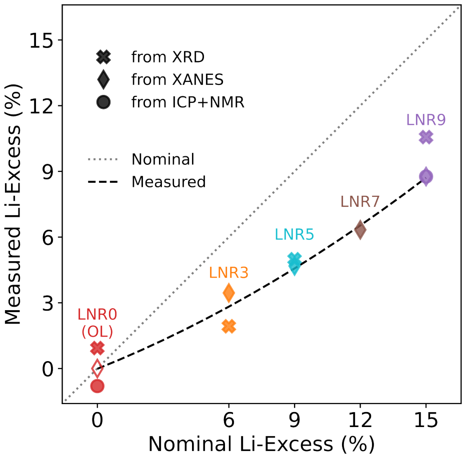

Supplementary Fig. 1 | Experimentally determined compositions for the electrochemically-active phase of as-synthesized pristine LNR*i* using various techniques. Nominal Li-excess (*j*) defined as follows: nominal Li/TM ratio = (1+*j*+0.01)/(1-*j*) in the reactant mixture. Measured Li-excess (*i*) defined as: $Li_{1+i}(Ni_{0.9}Mn_{0.1})_{1\text{-}i}O_2$.

Li-excess Mn-rich (LMR) cathode with composition $Li_{1.34}(Mn_{0.34}Ni_{0.66})_{0.66}O_2$ was used only as a reference in high-rate electrochemical test (Supplementary Information section 6.2). LMR was also prepared by co-precipitation followed by solid-state calcination. Co-precipitation was performed under nitrogen atmosphere in a continuously stirred tank reactor with constant temperature (45 °C). A 2.1 M solution of $NiSO_4$ and $MnSO_4$ (1:1.95 ratio) in deionized water was prepared and added to the reactor with precipitating solutions of 6.9 M NaOH and 0.93 M $NH_3 \cdot H_2O$. NaOH solution was used to maintain a reaction pH of 11.75. The precipitate was filtered and washed with deionized water until the conductivity of the filtrate was below 40 µS, yielding $(Ni_{0.34}Mn_{0.66})(OH)_2$ precursor. This precursor was dried, sieved, and then mixed with appropriate amount of Li_2CO_3. The reactant mixture was calcined at 925 °C (10 h ramp, 5 h dwell) under synthetic air to make $Li_{1.34}(Mn_{0.34}Ni_{0.66})_{0.66}O_2$.

1.2. Electrochemical measurements, and electrode harvesting.

To prepare the cathode electrode sheet, 80 wt% as-synthesized cathode active material (CAM), 10 wt% carbon black (Alfa Aesar Super P®), and 10 wt% polyvinylidene fluoride binder (Alfa Aesar) in N-methyl-2-pyrrolidone (Acros Organics) were mixed (Thinky mixer AR-100) and the resulting slurry was cast onto carbon-coated Al foil (MTI Corporation) using a doctor blade. The resulting sheet was dried at 100 °C on a hotplate inside an Ar-filled glovebox for 12 h and has cathode loading around 3 mg/cm^2. CR2032 coil cells (Wellcos) were assembled in an Ar-filled glovebox with 11.3 mm diameter cathode electrode, 25 µm thickness polypropylene/polyethylene/polypropylene separator (Celgard® H2512), 0.5 inch diameter Li foil anode (750 µm thickness, Sigma-Aldrich), and LP57 electrolyte (BASF SelectiLyte®, 1 M $LiPF_6$ in 3:7 wt/wt ethylene carbonate:ethyl methyl carbonate (EC:EMC)).

Electrochemical cycling tests were typically performed in the voltage range of 2.5–4.7 V *vs.* Li/Li^+ in constant current (CC)–constant voltage (CV) mode. The standard initial activation cycles are composed of C/20 CC charge with CV hold until C/50

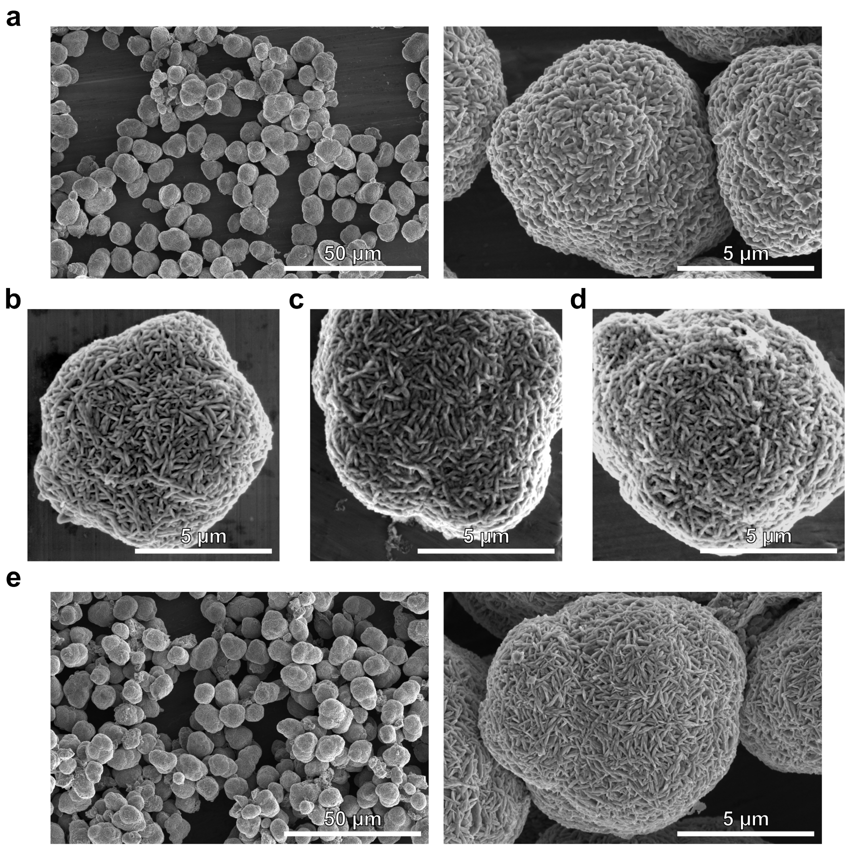

Supplementary Fig. 2 | a–e, SEM images of as-synthesized pristine LNR0 (OL) (**a**), LNR3 (**b**), LNR5 (**c**), LNR7 (**d**), and LNR9 (**e**).

current, and C/20 CC discharge with CV hold until C/500 current. 1C current is defined as 200 mA g^{-1} (with respect to nominal pristine CAM mass) in this work. For some tests, 2.5–4.3 V voltage window was also used together with 2.5–4.7 V cycles. Details of cycling conditions are specified in Supplementary Table 2 for *ex situ* characterized samples, and in relevant captions and texts for other samples whenever applicable. All coin cell cycling was conducted in a temperature chamber at 30 °C.

Cycled samples were harvested from coin cells dismantled using a decrimping instrument (MTI corporation) in a glovebox. All harvested electrodes were rinsed with dimethyl carbonate. The collected electrodes were used for the assembly of pouch cells (*operando* X-ray diffraction (XRD) and *operando* X-ray absorption (XAS)), the assembly of special coin cells (*operando* differential electrochemical mass spectroscopy (DEMS)), or some *ex situ* characterizations (XAS, and scanning electron microscopy (SEM)) directly. For other *ex situ* characterizations (inductively coupled plasma - optical emission spectroscopy (ICP-OES), ^{7}Li solid-state nuclear magnetic resonance (NMR), X-ray diffraction (XRD), and scanning transmission electron microscopy (STEM)), powder materials scraped off from the electrodes were used.

1.3. Cell fabrication for *operando* measurements.

Pouch cells for *operando* XRD and XAS measurements were prepared in a glovebox using polymer-cladded aluminum pouches. The main cell components are the same as in coin cells except that a thinner (500 µm) Li foil was used as the anode, and nickel (negative) and aluminum (positive) tabs were additionally used.

Half cells for DEMS were fabricated as CR2032 coin cells where a SUS mesh was used as the cathode current collector and a glass microfiber filter (Whatman® Grade GF/F) was used as separator for even gas delivery. A hole was made on the cathode-side cell cap to allow gas to pass through.

Cell cycling during all *operando* characterizations was carried out at room temperature, without the use of a temperature chamber.

1.4. Inductively coupled plasma - optical emission spectroscopy.

Sample digestion for ICP consisted of several steps. The sample was first mixed with nitric acid (HNO_3) and the resulting mixture was heated on a hot plate set to 180 °C for initial dissolution. When only a small amount of nitric acid remained, aqua regia (3:1 v/v HCl:HNO_3) was added and the resulting mixture was heated again at 180 °C on a hot plate. After the samples was completely decomposed by aqua regia, DI water was added to dilute the solution. The digested sample solution was then measured by ICP-OES (Perkin Elmer Optima 7000 DV ICP-OES).

1.5. ^{7}Li solid-state nuclear magnetic resonance.

^{7}Li solid-state NMR measurements were carried out at B_0 = 2.35 T (100 MHz for ^{1}H) using a wide-bore Bruker BioSpin spectrometer equipped with a DMX 500 MHz console and a custom-made 1.3 mm X-broadband magic angle spinning (MAS) probe tuned to ^{7}Li (38.9 MHz). Samples were packed into the 1.3 mm zirconia rotors inside a glovebox and closed with Vespel caps.

All spectra were acquired at 60 kHz MAS using dry nitrogen for spinning. ^{7}Li chemical shifts were externally referenced using 1 M aqueous LiCl solution ($\delta = 0$ ppm). All acquisitions were conducted using a rotor-synchronized spin-echo sequence and a 90° pulse of 0.45 µs. High sensitivity spectra were acquired using a 50 ms recycle delay that is sufficiently long for the ^{7}Li signals from the paramagnetic electrochemically-active phase to fully relax between scans, but leads to an underestimated ^{7}Li signal intensity. Quantitative (albeit lower sensitivity) spectra were also acquired using a longer, 10 s recycle delay allowing for both paramagnetic and diamagnetic signals to fully relax between scans. NMR data was processed using Bruker TopSpin 3.6.5 and spectral fits were conducted with DMfit[50].

1.6. X-ray diffraction.

Capillaries for powder XRD were prepared inside a glovebox by first compacting samples inside 'special glass' capillaries (Charles Supper) with the open end enclosed by vacuum grease. The capillaries were then immediately flame-sealed after being taken out of the glovebox. *Ex situ* powder XRD was measured in transmission geometry with spinning capillaries at either beamline 11-BM-B at the Advanced Photon Source (APS) in Argonne National Laboratory, or beamline 2-1 (with Dectris Pilatus 100K detector) at Stanford Synchrotron Radiation Source (SSRL) at SLAC National Accelerator Laboratory (see Supplementary Table 2 for details). NIST LaB_6 standard reference material was used to calibrate the instrument whenever appropriate.

Operando XRD was performed on pouch cells in transmission geometry with normal X-ray incidence to the electrodes either at beamline 11-3 at SSRL (12.7 keV X-ray, Rayonix MX225 detector, 18 cm sample-to-detector distance), at beamline 17-BM-B at APS (51.5 keV X-ray, Varex 4343CT detector, 100 cm sample-to-detector distance), or with Panalytical Empyrean diffractometer (line-focus Mo K_α X-ray source with focusing mirror optics, GaliPIX^{3D} detector in static line detector mode). Custom pouch cell holders were used where the electrode stack region of each pouch cell was pressurized between two thin beryllium plates to maintain pressure during electrochemical cycling while allowing for X-ray transmission[51]. For synchrotron measurement, to make up for the smaller beam size, the cells were oscillated perpendicular to the beam so that larger electrode areas were measured.

Integration of the raw diffraction images from synchrotron-based measurement to $I(2\theta)$ was done using either custom script (for SSRL 2-1 data) or pyFAI[52] (for everything else). Pseudo-Voigt single peak fitting (for **c**-lattice parameter determination from (003) peak), Pawley refinement (for lattice parameters determinations from whole pattern fitting), and Rietveld refinement (for structural analysis) were performed with Topas-Academic V7[53]. XRD data is plotted in Q-space as $I'(Q)$ that preserves integrated intensity according to $I'(Q)dQ = I(2\theta)d2\theta$ where $Q = 4\pi\sin(\theta)/\lambda$. The *ex situ* XRD patterns were also consistently scaled such that the integrated area for each peak is proportional to the structure factor between different samples.

1.7. X-ray absorption spectroscopy.

Ni K-edge XAS was performed in transmission geometry on electrodes (sealed inside pouches in an Ar-filled glovebox) at beamline 2-2 at SSRL. *Operando* Ni K-edge XAS was performed in transmission mode on pouch cells (same holder as described in Supplementary Information section 1.6) at beamline 2-2 at SSRL. Electrode surfaces were mounted at 45° to the incident X-ray beam. A Si(220) ϕ=90° monochromator was used. Detuning to about 60% maximum intensity was carried out to eliminate higher-order harmonics. Three ion chambers were used in series to simultaneously measure I_0 (incident X-ray intensity), I_1 (intensity post-sample), and I_2 (intensity post-sample and post-reference).

The spectra of Ni reference foil was used to calibrate the photon energy by setting the first crossing of zero of the second derivative of the absorbance spectrum to be 8333 eV. Spectrum normalization was performed with custom code using the same approach as implemented in the Athena software package[54]. A linear function was used for pre-edge fitting while a quadratic function was used for post-edge normalization fitting. The white-line energy of Ni K-edge is defined as the energy where the flattened normalized absorption spectrum reaches maximum. To reduce the impact of normalization parameterization, the final reported white-line energy is determined from the mean of 400 white-line energies calculated using different post-edge starting energies between $E_0 + 130$ eV to $E_0 + 330$ eV (E_0 is the first crossing of zero of the second derivative of the absorbance) with fixed post-edge ending energy and pre-edge range (because normalization result has greatest variance with the choice of post-edge starting energy).

1.8. Differential electrochemical mass spectroscopy.

Operando DEMS was performed using Hiden Analytical HPR-40 DEMS to track the oxygen (O_2) and carbon dioxide (CO_2) gas pressures during cell charging. Ar was used as the carrier gas (flow rate: 15 cc/min).

1.9. Scanning electron microscopy, ion milling, focused-ion beam (FIB) milling, and scanning transmission electron microscopy.

Regular secondary electron SEM images were recorded using Thermo Fisher Scientific Apreo S LoVac SEM in high-vacuum field-free mode with an Everhart-Thornley detector.

The cross-sectional SEM images in Fig. 2d (for charged samples) were produced via ion milling followed by field-emission SEM. The harvested electrode in the charged state was ion milled (Hitachi ArBlade 5000) to expose the cross-section. Backscattered electron images were acquired from a field-emission electron microscope (Hitachi Regulus 8230) using its YAG BSE detector.

The cross-sectional SEM images in Supplementary Fig. 13 (for lithiated samples) were produced via FEI Helios NanoLab 600i FIB/SEM system on sample electrodes. The electrodes were transferred from glovebox to the FIB/SEM system using a custom-built mechanical air-free sample transfer system. The sample electrode was tilted at 52° from being normal to the electron beam so that it was normal to the Ga^+ ion beam, which was used for sample sectioning and polishing. Secondary electron images were taken with the Elstar in-lens SE detector.

Samples for STEM imaging were sectioned using FIB (FEI Scios Microscope). General thickness of samples was between 70 and 100 nm over a range of several µm by Ga^+ ion milling. A preliminary milling step involving a platinum-based wedge was employed to maintain the integrity of the protective surface layer throughout the milling process. An aberration-corrected (scanning) transmission electron microscope (FEI Titan$^{3\text{TM}}$G2 60-300 S/TEM) was used to obtain Cs-corrected STEM images with atomic resolution at 60 and 100 kV acceleration voltage. Line intensity profiles and fast Fourier-transform (FFT) images were obtained using Fiji ImageJ[55].

The high-resolution STEM images presented in Fig. 1e–g are cropped in size for improved readability, while the line profiles and FFT images were obtained from the original images of size 9.31×9.31 nm^2.

2. Supplementary Notes

2.1. Partial disorder in layered oxide cathodes.

Although too much Li–TM antisite disorder can cause detrimental effects to the capacity and cyclability of layered oxide cathodes, we believe cathode capacity at slow (de)lithiation rate would depend little on the extent of cation disorder.

The theoretical capacity of O3-type layered oxide cathode can be affected by total Li concentration and percolation of Li migration channels. Paired antisite $[(\mathrm{Li}_{1\text{-}a}\mathrm{TM}_a)_{\mathrm{Li}}(\mathrm{TM}_{1\text{-}a}\mathrm{Li}_a)_{\mathrm{TM}}\mathrm{O}_2]$ does not change the amount of Li in the cathode, so the Li concentration would remain the same. For the Li to be able to contribute to ionic current (active Li), it also needs to be within a percolating migration channel. In O3-type layered cathode, oxygen anions are packed into face-centered cubic (FCC) arrangement, which leaves behind FCC octahedral sites where Li, TM, or vacancy can reside. Li diffusion proceeds via vacancy-mediated migration between neighboring octahedral sites, passing through the tetrahedral interstice. Assuming TM is immobile, active Li has to be within a percolating channel of connected octahedral sites of Li or vacancy, and not within a finite isolated cluster bound by TM atoms. Simulations based on percolation theory suggests that for a completely disordered rock salt structure (whose spatial geometry of anion and cation sites are the same as O3) having $\mathrm{Li}_{1\text{-}\beta}\mathrm{TM}_{1+\beta}\mathrm{O}_2$ composition, the fractional percolating Li (*i.e.* $\mathrm{Li}_{\mathrm{percolating}}/\mathrm{Li}_{\mathrm{total}}$) is almost 100% for $\beta \leq 0.2$[56]. Even for $\beta = 0.4$, the fractional percolating Li is >95%. We are unaware of similar percolation simulations for Li-stoichiometric layered oxide with partial disorder, but if both in-plane and out-of-plane Li migration are possible and there is no effect favoring short-range ordering or clustering, then it is possible the fraction of percolating Li can remain close to 100% for moderate antisite amount (<20%). This implies the theoretical capacity is not impacted by partial disorder.

However, practical capacity for partially disordered cathode can be affected due to the reduction of Li diffusivity. The impact of this will be more severe at high charge/discharge rates. It is shown that Li migration is limited by the electrostatic repulsion experienced when it is at the intermediate tetrahedral sites. This repulsion depends strongly on the local number of face-sharing high-valent TMO_6 octahedra (which gives rise to the distinction of 0-TM, 1-TM, 2-TM channels) and the size of the tetrahedral interstices[56–58]. For perfectly ordered layered oxides, Li migration occurs exclusively through the 1-TM channels within the Li layers. Perhaps the biggest impact of partial cation disorder is the reduction of the Li layer height, which in turn reduces tetrahedral size in the Li layer and increases the migration barrier of the 1-TM channel. This argument implies a negative relationship between the extent of cation disorder for layered oxide and its rate performance.

2.2. Lattice parameter evolution during (de)lithiation in O3-type layered cathodes.

Layered oxide cathodes for lithium-ion battery (LIB) application most commonly have the O3 structure (LiTMO_2), which consists of FCC packing of oxygen ions with octahedral interstices occupied by Li and TM ions separating into alternating Li and TM slabs[59]. Changes to the lattice parameters during electrochemical (de)lithiation of O3-type layered cathode ($\mathrm{Li}_x\mathrm{TMO}_2$) with different compositions have been reported and are well understood[2–4]. Both **a** and **c** lattice parameters (representing in-plane and out-of-plane dimensions, respectively) show a turning point at a critical value of x_{Li} within 0.4–0.5. Here we use the term 'shallowly delithiated' to denote states where x_{Li} is bigger than the critical value and 'deeply delithiated' to represent where x_{Li} is smaller than the critical value. In the shallowly delithiated state, with delithiation, **a** decreases slightly and **c** increases. In the deeply delithiated state, with delithiation, the rate of decrease in **a** slows down, and depending on the specific composition, can even become nearly constant or slightly increasing[2]. The changes in **c** in the deeply delithiated state are very dramatic, plunging with delithiation and causing severe **c**-collapse regardless of the exact composition. More than 5% change in **c** can happen within an x_{Li} range of 0.3. Overall, changes in **a** are much smaller than **c**. The strain differential between different crystallographic directions causes large anisotropic strain, leading to particle shape change, intra- and inter-particle cracking[7,60].

Changes along the in-plane **a** direction can be understood well by considering TM–O bonding alone[4]. With delithiation, TM ions are oxidized to higher average valences. Since the ionic radius for TM decreases with oxidation state, TMO_6 octahedra is expected to contract, resulting in smaller **a**. The change of slope in **a** *vs.* x_{Li} entering the deeply delithiated state can be rationalized by a change in the nature of TM–O bonding. It is suggested that charge transfer from O to TM happens at deeply delithiated state, which increases the covalency of TM–O bonds and thus alters the behavior of the TMO_6 size.

Changes along the out-of-plane **c** direction is a combined result of the slab thickness changes for the TMO_6 slab and the LiO_6 slab[4]. The overall trend of TMO_6 slab thickness is similar to in-plane **a** dimensional changes and can be rationalized by the decrease in TM ionic radii as TM get oxidized. The decrease in TMO_6 slab thickness does not obviously slow down when entering the deeply delithiated state[4], implying less impact of TM–O bond along this direction. The variation of TMO_6 slab thickness due to TM oxidation is smaller in magnitude compared to that of LiO_6 slab thickness during (de)lithiation. Thickness of the LiO_6 slab is strongly affected by the electrostatic repulsion between its upper and lower O ion layers. Li^+ ions provide screening to the electrostatic repulsion between O layers. In the shallowly delithiated state, as Li^+ is removed, the strength of screening decreases, so the effective repulsion between O layers increases, leading to increase in LiO_6 slab thickness. In the deeply delithiated state, because of the increased covalency character in TM–O bonds, oxygen ions are less ionic and the intrinsic repulsion strength between O layers quickly fades[3,61]. The repulsion strength decreases sharply with a small change on nominal TM oxidation state (and hence Li concentration), which manifests as a sharp decrease in LiO_6 slab thickness with delithiation. In this deeply delithiated state, both TMO_6 and LiO_6 slab decrease in thickness, resulting in a plunge of the value of **c** (**c**-collapse). Furthermore, as **a** stops to decrease (either decreases little or increases) at this stage, the disparity among the in-plane and out-of-plane directions gives rise to large strain anisotropy. Many practical cathodes have a microstructure of secondary particles consisting of an agglomerate of primary particles[16,62]. With the primary particles randomly oriented, large anisotropic strain will cause grain separation between primary particles, exposing fresh surfaces to electrolyte. Coupled with surface-reactivity with electrolyte, this leads to the formation of microcracks inside the secondary particle[6,7].

We note that all the above discussions on lattice parameter evolution are for when the material can still maintain an O3 structure. If **c** (more correctly LiO_6 slab) has collapsed significantly, oxygen p orbitals from adjacent layers will overlap. To minimize the direct interaction between O $2p$ orbitals, oxygen stacking will change to O1-type[63,64]. This O3–O1 transition involves shear and gliding of the oxygen layers, which is detrimental to LIB performance. Local generation of O1 domains has been observed in deeply delithiated layered cathodes having the O3 matrix[65]. O1 has even smaller **c**, and therefore its presence can also appear as continued reduction in **c** seen from diffraction. This is because it is difficult to differentiate between O1-structure (also referred to as H4 phase for Ni-rich cathodes) signals from O3-structures (referred to as H1, M, H2, and H3 phases for Ni-rich cathodes)[5].

Suppression of the collapse of LiO_6 slab can mitigate all the above-discussed negative impacts (particle shrinkage, anisotropy, O1 formation). The presence of other ions within the Li layer have been shown useful in this regard[8–10]. We believe there are two primary contributing factors. The first is that in the deeply delithiated state where the Li layer is very cation-vacant, there is no hindrance to the collapse of LiO_6 slab until O $2p$ orbitals starts to overlap. The presence of immobile ions within the Li layer can provide steric support against the collapse. The second is that the large partial (Li) molar change of LiO_6 thickness is related to the weak screening of the electrostatic repulsion across Li layer. Therefore, a small change of the screening strength or oxygen ionicity will have a big impact on LiO_6 slab thickness. With high-valent TM ions within the Li layer, the screening is much stronger such that, with the same change of Li content, the fractional change of effective electrostatic repulsion between O becomes less pronounced. These arguments suggest that a moderate concentration of TM_{Li} is effective to reduce cycling strain in O3-type layered cathodes.

Additionally, TM ions within the Li layer inhibit O3–O1 transition. Shear and glide between oxygen layers are necessary for this structural transition, whose pathway are kinetically obstructed if the Li layers are not vacant due to the additional need to displace cations. Thermodynamic free energies of hypothetical O1 structures with TM in the Li layer will also be very high, since O1 arrangement minimizes the orbital overlap between O but are extremely unfavorable for the interaction between O and cations in the Li slab[64].

2.3. Composition of the electrochemically-active phase of cathode.

Cathode active material (CAM) is a commonly-used term in LIB industry to refer to the ingredient responsible for electrochemical capacity before the mixing and casting of the cathode electrode sheet. The term ‘active’ here is used to distinguish this ingredient from the other ingredients that are necessary to form a functional electrode sheet but do not contribute to electrochemical reactions (*e.g.*, conductive additive, binder, current collector). However, this CAM ingredient itself typically contains complex combinations of chemical phases and interphases, not all of which are electrochemically active. For example, Li_2CO_3 is a common impurity residue. Surface treatment methods can also produce interphases that do not directly participate in redox reactions. In this work, the term ‘electrochemically-active phase’ is used to refer to the subset phase(s) of cathode containing the redox-active elements of concern. With this definition, for a TM oxide-based cathode, the electrochemically-active phase contains all TM elements, whereas the total Li within cathode can be spread between the active phase and inactive phases.

The determination of the chemical composition of only the electrochemically-active phase is important, because it is fundamentally the amount and properties of the electrochemically-active phase that determine the theoretical capacity, equilibrium voltage, and reversibility of LIB cathode. However, it is challenging to experimentally isolate the electrochemically-active phase, and most cathode analyses are performed on the aggregated CAM or electrode mixture. One typical example is ICP-based chemical analysis, which can provide the ratio between elements in the aggregated CAM, but usually not directly for the electrochemically-active phase. In cases where composition of the electrochemically-active phase differs from that of the aggregated CAM, this can lead to misinterpretations. For example, a cathode formulation having an aggregated Li:TM mol ratio close to 1.00:1.00 may be made up of a mixture of Li-deficient electrochemically-active phase ($Li_{1-\beta}TM_{1+\beta}O_2$, which contains a lot of TM_{Li} due to Li-deficiency) and Li_2CO_3. Its capacity is likely smaller than anticipated based on analyses of the aggregated CAM because its electrochemically-active phase has less Li. However, the reduced capacity may be falsely attributed on TM_{Li} antisite if composition of the electrochemically-active phase is not robustly determined.

2.4. The influence of cathode composition on electrochemical behavior.

2.4.1. Li-stoichiometry, redox mechanisms and capacities.

The redox mechanisms and capacities are highly affected by the amount of Li in the electrochemically-active phase of a cathode. For a lithium TM oxide with O3-type structure, its general composition can be expressed as $Li_{1+\gamma}TM_{1-\gamma}O_2$ assuming there is no cation or oxygen vacancy in the structure. For common TM used in LIB cathodes such as Ni, Co, and Mn, the maximum oxidation state attainable within a practical voltage limit is 4+. During delithiation, TM ions are gradually oxidized to approach this limit, where the electrons within the hybridized antibonding TM $3d$–O $2p$ band (hereafter referred to as TM $3d$ band) are depopulated. The energy of the unhybridized O $2p$ band is overall lower, and therefore O oxidation only occurs at a higher voltage after nearly all TM have been oxidized to 4+ oxidation state (for TM such as Ni and Co, there may be a small extent of band overlap between the bottom of TM $3d$ band and the top of the unhybridized O $2p$ band). Oxidized oxygen in oxide cathode have been suggested to take the form of localized hole states[66,67], delocalized hole states[68–70], peroxide- and superoxide-like oxygen dimers[71,72], and molecular O_2 trapped in the bulk[28,31,73]. For simplicity, here we proceed by not differentiating between the different forms of oxygen redox and also assuming there being no band overlap between TM $3d$ and unhybridized O $2p$. In this simple picture, TM and O redox take place sequentially and reversibly.

For a stoichiometric $Li_{1.0}TM_{1.0}O_2$, TM has an initial average oxidation state of 3+, and the complete delithiation can perfectly be charged compensated by TM being oxidized to the maximum oxidation state of 4+.

For a Li-deficient $Li_{1+\gamma}TM_{1-\gamma}O_2$ ($-1 < \gamma < 0$), the theoretical capacity is limited by the available Li. Even at full delithiation, TM has yet to reach the maximum average oxidation state of 4+.

For a Li-excess $Li_{1+\gamma}TM_{1-\gamma}O_2$ ($0 < \gamma \leq 1/3$), the Li capacity exceeds TM-redox capacity. The reduction of TM-redox capacity with Li-excess is due to combined effect of having a smaller TM concentration and the starting average oxidation state for TM in the pristine state being higher. For these materials, when TM are already oxidized to the maximum oxidation state of 4+, there remains extra Li in the electrochemically-active phase. In principle, with increased potential, extra Li can be removed by depopulating the unhybridized O $2p$ band, giving rise to O oxidation. With this treatment, the theoretical capacity for $Li_{1+\gamma}TM_{1-\gamma}O_2$ can be calculated and broken down into partitions between cation-redox and oxygen-redox (Supplementary Fig. 3). As can be seen, when Li goes beyond stoichiometric, cation-redox capacity decreases even though the Li-based capacity can increase, with the gap being potentially satisfied by anion-redox. A higher Li-excess is expected to trigger a greater extent of anion-redox with this simplified treatment.

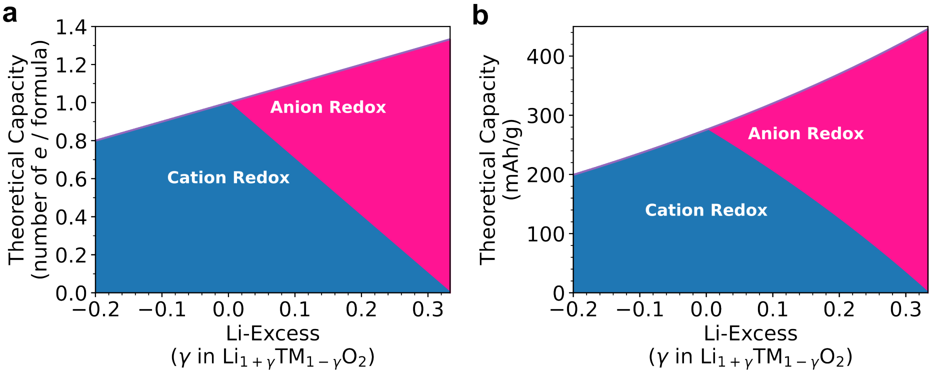

Supplementary Fig. 3 | a,**b**, Theoretical molar capacity (**a**) (expressed as number of elementary charge per formula unit) and specific capacity (**b**) (with TM = $Ni_{0.9}Mn_{0.1}$) for layered lithium transition metal oxide cathode, and the breakdown of the total capacity into cation-redox capacity (blue) and anion-redox capacity (pink) with the simplified assumption that the two mechanisms are completely sequential with no energy overlap between $TM^{4+}/TM^{3+}/TM^{2+}$ couples and O 2*p* bands.

2.4.2. Systems suitable for oxygen oxidation-induced structural activation.

Real systems with anion-redox are more complicated than Supplementary Fig. 3 implies. Alternative processes may interfere with anion redox (*e.g.*, oxidation of other battery components such as electrolyte at such high potentials). The electrochemically-active phase of the cathode itself may also undergo chemical and structural changes during the oxidation and reduction of oxygen, making the process irreversible[74]. A widely studied anion-redox system is the Li-excess Mn-rich (LMR) cathodes[17,18,75], which have been shown to have partially reversible collective TM migration during every electrochemical cycle. The observed coupling between structural evolution and O-redox inspired us to seek possibilities where O oxidation can be used as an activator to induce structures with new atomic arrangements.

In contrast to the research focusing on stabilizing and improving the reversibility of O-redox, here we aim to have very irreversible processes so that the evolved structure can stabilize quickly. This allows the possibility of releasing gas-phase activation by-products (*e.g.*, O_2) in a single degassing step (after formation/activation) before final sealing if a large-format full cell is to be fabricated. Ni-rich cathode is identified to be one such potential candidate.

We speculate Li-excess Ni-rich cathodes are more prone (compared to Mn-rich cathodes) to the release of its lattice oxygen as O_2 gas after the oxidation of oxygen anions. This speculation is based on the consideration of relatively stronger covalency (weaker ionicity) character of the Ni–O bonds. The covalency feature in the nominally ionic Ni–O bond manifest as ligand holes ($\underline{L}$), also called ‘negative charge transfer’ ground states of the Ni^{3+} ($3d^8\underline{L}$) and Ni^{4+} ($3d^8\underline{L}^2$) ions[76]. The presence of ligand holes has been suggested in pristine and delithiated $LiNiO_2$[61,77,78]. Because of this, there is a greater electron hole density near O along the O–Ni bond direction. We postulate that oxygen anion coordinated with Ni (and additionally contains unhybridized O 2*p* band, *i.e.*, with ≈180° Li–O–Li configuration) has a greater tendency to decoordinate with TM if oxygen oxidation depopulates electrons from its unhybridized O 2*p* band, leading to irreversible O_2 release and TM migration. In this work, we experimentally demonstrate such phenomena by showing the activation outcome of as-synthesized Li-excess Ni-rich cathodes upon initial cycling, leading to the formation of a partially disordered layered structure.

3. Supplementary Discussion: Composition and Structural Analyses

Three types of independent techniques based on entirely different physical principles were deployed to determine the composition of the electrochemically-active phase of cathode: coupled ICP+NMR, XRD, and XANES. Additionally, XRD provides information relating to the structural disorder.

3.1. ICP+NMR.

In the ICP+NMR method (Supplementary Table 1), we first used ICP-OES to determine the overall Li:TM (TM = Ni + Mn) atomic ratio in the entire aggregated cathode (Ni:Mn ratios determined from the ICP were very close to the expected ratio of 9:1). It is expected that TM atoms reside almost exclusively within the electrochemically-active phase of the cathode. However, Li signals from ICP can have two origins: Li within the electrochemically-active phase, and Li in other inactive components (such as Li impurities (*e.g.*, Li_2CO_3) or surface coating layers (*e.g.*, $LiBO_2$)).

To differentiate between the two types of Li, we further performed ^{7}Li solid-state NMR measurements on the samples of interest to differentiate the Li in the potential diamagnetic (containing no Ni or Mn) auxiliary phases and in the paramagnetic (Ni and/or Mn containing) electrochemically-active phase.

^{7}Li solid-state NMR spectra collected on pristine LNR0 and LNR9, as well as on *ex situ* samples after various number of cycles are shown in Supplementary Fig. 4. All spectra feature a sharp 0 ppm signal characteristic of diamagnetic Li environments in auxiliary (inactive) phases in the sample. These auxiliary phases likely include Li_2CO_3 observed by XRD for the pristine samples, $LiBO_2$-like glassy surface coatings, and electrolyte decomposition products for samples scrapped of from the cycled electrodes. In contrast, ^{7}Li NMR signals arising from Li species in the electrochemically-active phase of cathode are expected to be significantly broadened and shifted away from 0 ppm, due to the strong hyperfine interactions between the paramagnetic species (here, Ni^{2+}, Ni^{3+}, and Mn^{4+}) and the ^{7}Li nucleus under consideration. In these systems, the dominant source of chemical shift is the Fermi contact shift, which arises from the delocalization of unpaired electron spin density from the Ni/Mn d orbitals to the Li s orbital via bridging O p orbitals. The sign and magnitude of the Fermi contact shift contributions depend on the nature of the paramagnetic TM, and the overlap of the TM d, O p, and Li s orbitals (*i.e.*, TM–O, O–Li bond lengths, and TM–O–Li bond angles), providing detailed insights into the local structure. For LNR0 (Supplementary Fig. 4a), the presence of several Li environments in the Li layers gives rise to several broad and overlapping resonances that lead to an overall broad and asymmetric signal spanning a wide frequency range from 0 to +1000 ppm, and peaking around 670 ppm. Minimal changes in lineshape are observed after 100 cycles, indicating that the ordered layered structure is largely preserved. For as-synthesized LNR9 (Supplementary Fig. 4b), a broad and asymmetric ^{7}Li signal is observed over a similar frequency range, peaking around 590 ppm, indicating the presence of a number of unique Li chemical environments in the Li layers, with a slightly different distribution than for LNR0. An additional, relatively sharp peak can be observed at 290 ppm, which we attribute to Li in the TM layers (Li_{TM}) based on prior work on Li-rich nickel oxides ($Li_{1+\gamma}Ni_{1-\gamma}O_2$) indicating that the intensity of ^{7}Li NMR signals in the range of 200 ppm to 400 ppm scales with Li_{TM} content[22]. The sharpness of the signal may be related to the in-plane ordering of the Li_{TM} species, which is also consistent with the superstructure peaks in the XRD data (Supplementary Fig. 7a inset). The intensity of this 290 ppm peak in LNR9 is in the range of 5–11% of the total paramagnetic NMR signal intensity, consistent with the LNR9 composition determined by other methods and shown in later sections (Supplementary Table 5). After activating LNR9 to DL(9), the 290 ppm peak becomes broader, and gradually fades away upon extended cycling. This is likely related to the loss of in-plane Li–TM ordering with electrochemical cycling[28], resulting in more diverse local chemical environments for the different Li_{TM} ions, as well as potential depopulation of those Li_{TM} sites. In contrast, the broad and asymmetric signal attributed to Li in the Li layers does not evolve significantly during the activation cycle nor upon extended cycling, suggesting that most of the changes to the distribution of Li environments take place in the TM layers.

The molar fraction of Li in the electrochemically-active phase of cathode, for each of the samples listed in Supplementary Table 1, was quantified from a fit of their respective ^{7}Li NMR spectra obtained using a long recycle delay of 10 s, ensuring that both paramagnetic and diamagnetic signals could fully relax between scans. The total paramagnetic integrated ^{7}Li signal intensity (I_{para}) was obtained by summing over 2–3 broad signals needed to capture the lineshape of the broad resonance (an example is shown in Supplementary Fig. 4c for pristine LNR9), while the total diamagnetic integrated ^{7}Li signal intensity (I_{dia}) could be captured using a single component in the fit. Both diamagnetic and paramagnetic integrated signal intensities were then adjusted to account for the fact that the paramagnetic signals decay significantly faster than the diamagnetic signal(s) over the duration T of the measurement, due to their shorter spin-spin relaxation time ($T2$'). The fraction of Li in the electrochemically-active phase of cathode was then obtained by computing the ratio: $I_{para} * \exp(\frac{T2'_{para}}{T})/(I_{para} * \exp(\frac{T2'_{para}}{T}) + I_{dia} * \exp(\frac{T2'_{dia}}{T}))$, where $T2'_{para}$ is the average $T2$' decay time of the paramagnetic components, and $T2'_{dia}$ is the $T2$' decay time of the diamagnetic component.

Combining ICP-OES and ^{7}Li NMR quantifications, the atomic ratios of Li:TM in the electrochemically-active phase of cathode can be obtained (Supplementary Table 5). We emphasize here that to assure the validity of this coupled ICP+NMR method for composition determination, we made sure that for each sample, powder from the same exact batch was used for both ICP and NMR measurements.

For pristine LNR9, the coupled ICP+NMR composition quantification was repeated three times, and the results consistently yielded a stoichiometry within $Li_{1.088\pm0.010}TM_{0.912\mp0.010}O_2$. ICP+NMR is an overall more accurate composition determination method (than XRD Rietveld refinement, due to non-trivial correlation coefficient (≈ -50%) between stoichiometry and TM_{Li} concentration), and the pristine LNR9 composition obtained using ICP+NMR, of $Li_{1.088}TM_{0.912}O_2$, was used for our calculations later.

Supplementary Table 1 | Results of ICP-OES and paramagnetic Li quantification from ^{7}Li NMR

Sample description	ICP-OES result n / ($n_{\text{total Li}}$+n_{Ni}+n_{Mn})×100%			^{7}Li NMR result (paramagnetic Li) / (total Li)×100%
	total Li	Ni	Mn	
OL (LNR0) pristine	50.78%	44.93%	4.29%	95.37%
LNR9 pristine	56.80%	38.52%	4.68%	90.66%
DL(9) LNR9 after 1 cycle	53.39%	41.45%	5.16%	86.07%
DL(9) LNR9 after 2 cycles	54.20%	40.80%	5.00%	86.02%
DL(9) LNR9 after 5 cycles	56.73%	38.90%	4.37%	79.34%
DL(9) LNR9 after ≈100 cycles (4.7 → 4.3 V)	55.04%	40.43%	4.53%	84.80%

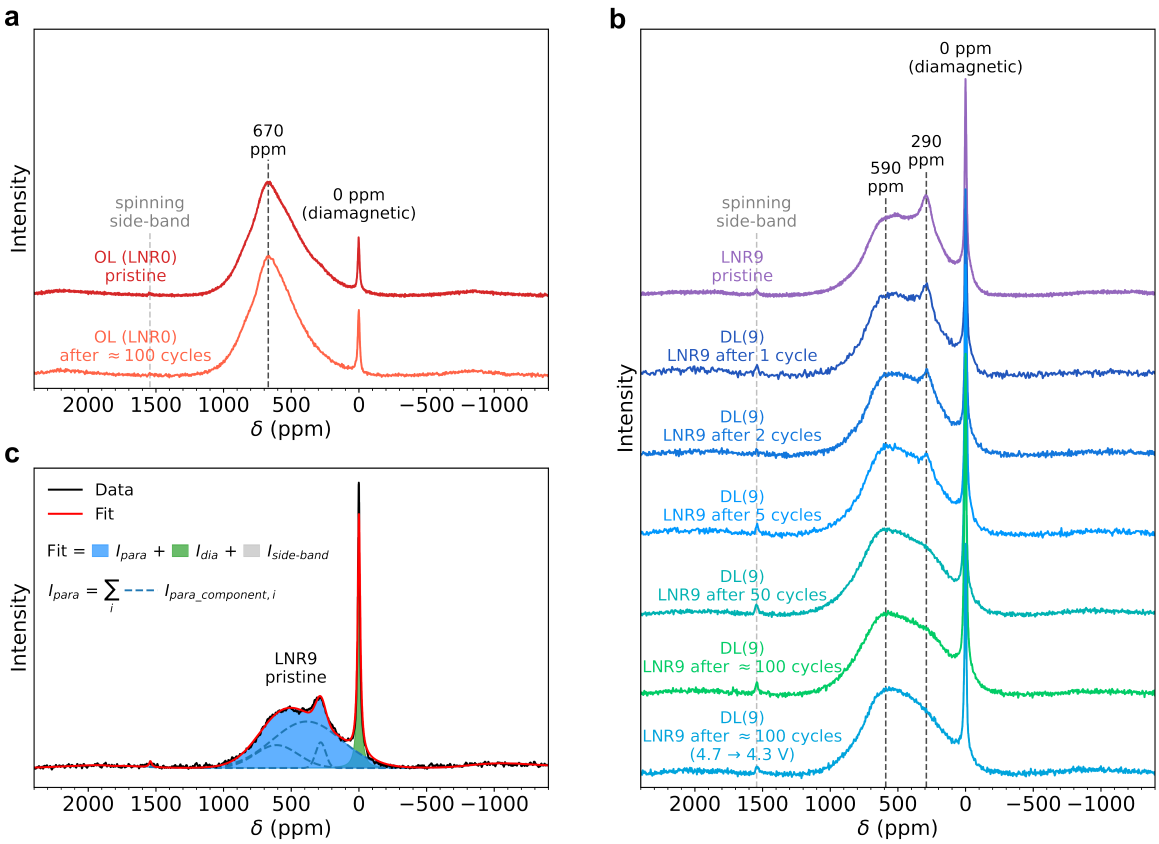

Supplementary Fig. 4 | a,**b**, ^{7}Li NMR spectra for pristine and cycled OL (LNR0) (**a**), and pristine LNR9 and cycled DL(9) (**b**) obtained at 2.35 T and at 60 kHz MAS, with a recycle delay of 50 ms to maximize sensitivity. **c,** An example spectrum for pristine LNR9 collected with a recycle delay of 10 s, and the breakdown of components used for its fit, illustrating the quantification method used to obtain molar fractions of Li in the electrochemically-active phase of cathode shown in Supplementary Table 1.

3.2. XRD refinement.

XRD and its Rietveld refinement (Supplementary Figs. 5-7, Supplementary Table 2) were used to infer the composition and purity of the as-synthesized as well as cycled cathodes. Because of crystal structure and hence lattice plane spacing differences, phases in the cathode other than the electrochemically-active phase generally do not interfere with the refinement confined to the Q-ranges of the Bragg peaks of the electrochemically-active phase. This crystallographic selectivity makes it viable to extract the information pertaining only to the electrochemically-active phase of cathode via Rietveld refinement.

All as-synthesized LNRi (i = 0, 3, 5, 9) samples show XRD patterns whose main peaks can be indexed to a-$NaFeO_2$ structure type with $R\bar{3}m$ space group, which is also referred to as O3-type structure of layered oxide[5,79]. After electrochemical cycling, all samples maintain the same $R\bar{3}m$ space group symmetry. Some extremely tiny and broad peaks can be identified that can be accounted for by small Li_2CO_3 impurity particles, which is consistent with the presence of diamagnetic ^{7}Li signals in the NMR data (Supplementary Table 1). No other peaks (other than the superstructure peaks for LNR9 to be discussed later) can be identified for all pristine and cycled samples. This suggests the absence of a secondary component (such as surface rock salt[22] or bulk heterostructure[10]) in all samples investigated in this study.

For LNR9, additional weak peaks can be seen in the Q-range of 1.4–2.0 Å^{-1}(Supplementary Fig. 7a inset), which are superstructure peaks resulting from extra symmetry due to in-plane ordering of atoms[22]. Such in-plane ordering is likely between Li and TM atoms within the TM layer, and the superstructure peaks being noticeable only in LNR9 is consistent with it having the highest level of Li-excess as determined by methods using other principles (summarized later in Supplementary Table 5). The superstructure peaks fade away after cycling (Supplementary Fig. 7c-h).

The presence of the superstructure peaks indicates that the symmetry for the materials is more accurately presented by $C2/m$ space group[22]. However, because superstructure peaks observed in this work are all very small, the effects of in-plane ordering on the structure factors of the main peaks will be negligible (much less than uncertainties introduced by other factors we are concerned with in this work such as overall composition and out-of-plane disorder). Therefore, Rietveld refinement performed with crystal structure models using $R\bar{3}m$ space group is a valid approximation.

All Rietveld refinements were performed based on $R\bar{3}m$ crystallographic construction of the electrochemically-active phase. If superstructure or Li_2CO_3 peaks are noticeable, the regions around them were excluded during the actual refinements so that they do not interfere with background fitting. X-ray wavelength and convolution terms related to instrument broadening were determined based on calibration XRD patterns collected on NIST standard materials and were fixed for the refinement of samples. For each sample, Pawley refinement was first performed to obtain lattice parameters and other convolution terms (size and strain broadening, peak shape function, and anisotropic broadening) that modulate peak profile but do not impact structure factors. After that, initial Rietveld refinement was conducted by only refining variables defining the crystal structure (atomic displacement parameters were refined and were constrained to be the same for different ions occupying the same crystallographic site). The final Rietveld refinement was performed where all applicable variables of the sample were refined. The crystal structures for all lithiated samples are assumed to have no vacancies (for both anion and cation sites). Li is allowed to reside within both the Li layer (3b site) and the TM layer (3a site). Both Ni and Mn are allowed to reside within TM layer, but only Ni is given the freedom to reside within Li layer (due to Ni having closer ionic radius to Li). (The TM_{Li} results won't change much if Mn is additionally allowed to be within the Li layer since the atomic scattering factors for Ni and Mn are similar.) Other than fixing total Ni:Mn ratio to be 9:1, no other chemical constraints are put into place. This allows the structure to freely converge with all possible Li:TM ratios to give an estimate on the composition of the electrochemically-active phase of cathode.

The fit for LNR9 after 1st charge was handled by constructing a Li-free structure having total Ni and Mn atoms per unit cell (*i.e.* TM:O ratio) the same as found in the relithiated sample (*i.e.*, LNR9 after 1 cycle). Because of the possibility of O_2 release during discharge of the first LNR9 activation cycle, the fixed TM:O ratio employed in the model may deviate slightly from the accurate value, but its associated uncertainty in TM_{Li} shouldn't exceed 0.02.

The results of Rietveld refinement are shown in Supplementary Table 3, from which information on lattice parameters, chemical composition, and the concentration of TM_{Li} antisite can be obtained. For pristine LNRi, a higher refined Li stoichiometry is found to correlate with a smaller unit cell volume, consistent with the previous relationship established for lithium nickel oxide cathode chemistry[5]. Some small extent of cation disorder ($<$ 7% TM_{Li}) exists even in the pristine LNRi samples, which has been a common observation for as-synthesized Ni-rich cathodes (due to the similar ionic radius between Ni^{2+} (0.69 Å) and Li^{+} (0.76 Å))[5,13]. After cycling, little changes happen to LNR0 and it remained fairly ordered. For LNR5 and LNR9 after 4.7 V upper cut-off voltage (UCV) cycling (*i.e.* DL(5) and DL(9), respectively), refinement results suggest decreases in unit cell volume, decreases in Li stoichiometry, and increases in TM_{Li} concentration. Changes in the first cycle are far more substantial than that in future cycles.

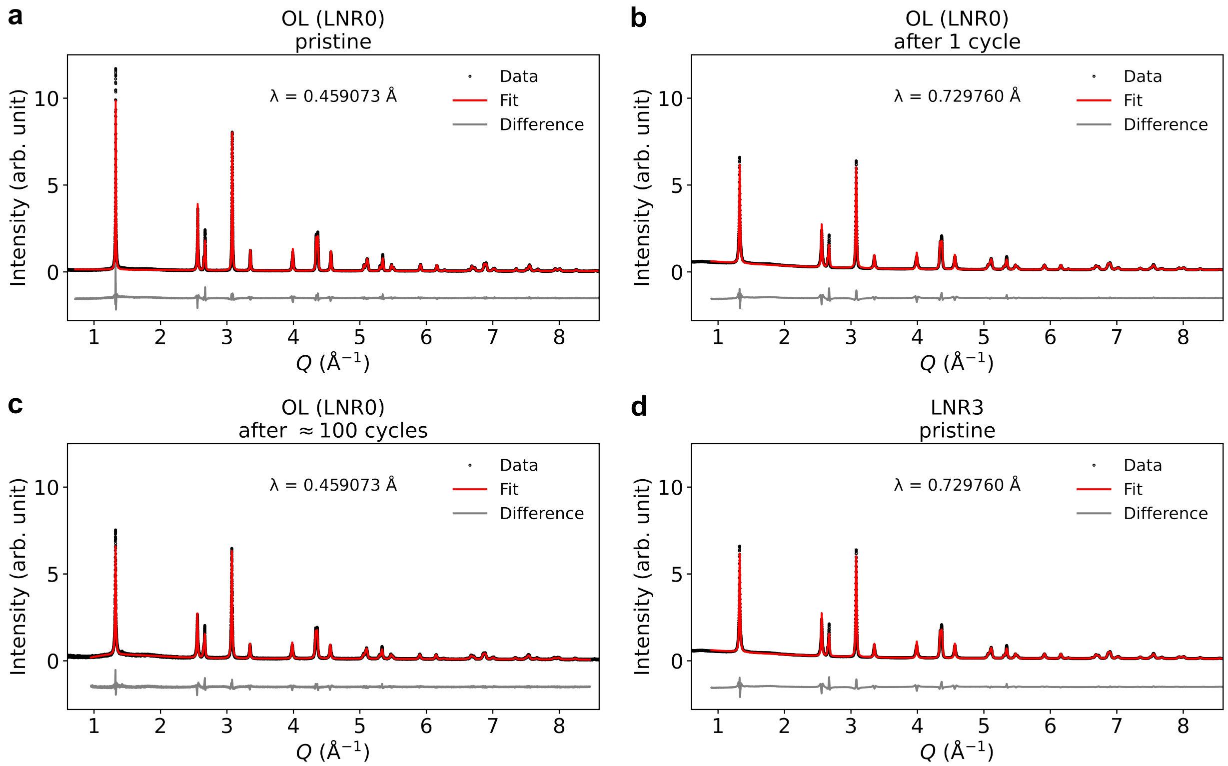

Supplementary Fig. 5 | **a**–**d**, XRD patterns and Rietveld refinement fits for OL (LNR0) in its pristine state (**a**), after 1 cycle (**b**), and after ≈100 cycles (2.5–4.7 V) (**c**), and for LNR3 in its pristine state (**d**).

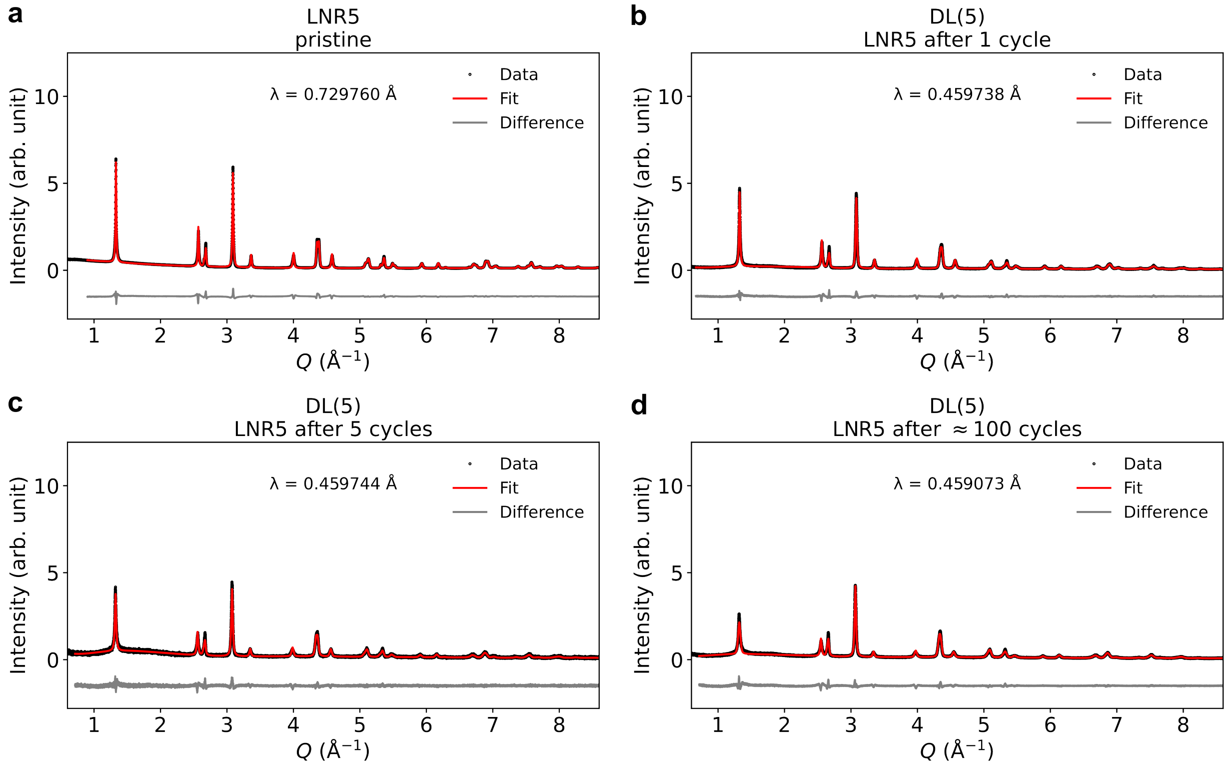

Supplementary Fig. 6 | **a**–**d**, XRD patterns and Rietveld refinement fits for LNR5 in its pristine state (**a**), and for DL(5) underwent 1 (**b**), 2 (**c**), and ≈100 total cycles (2.5–4.7 V) (**d**). Cycle number counting starts from pristine LNR5.

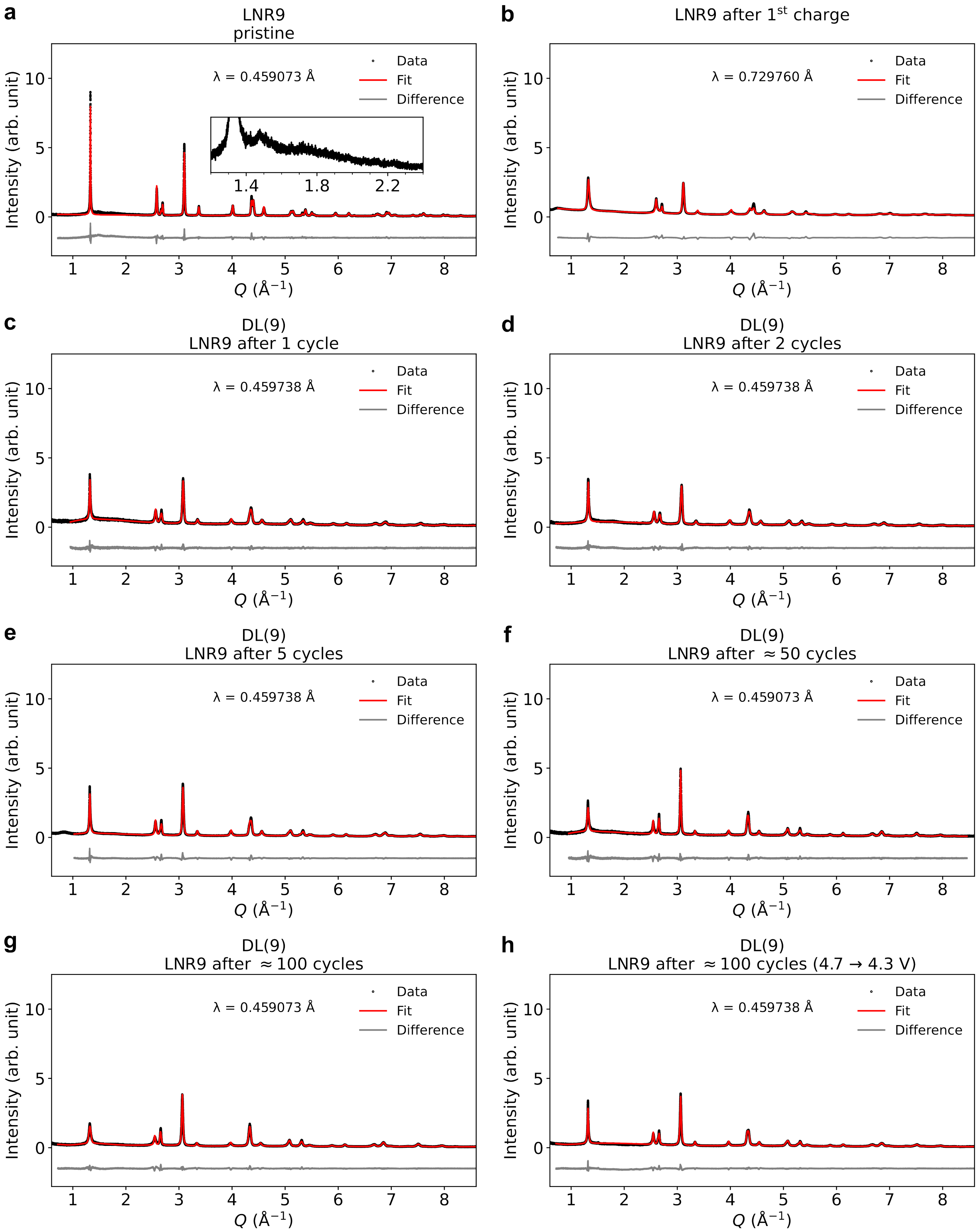

Supplementary Fig. 7 | **a**–**h**, XRD patterns and Rietveld refinement fits for LNR9 in its pristine state (**a**), for LNR9 after first charging (**b**), and for DL(9) underwent 1 (**c**), 2 (**d**), 5 (**e**), 50 (**f**), ≈100 total cycles (2.5–4.7 V) (**g**), and ≈100 total cycles (5 cycles in 2.5–4.7 V and the rest in 2.5–4.3 V) (**h**). Cycle number counting starts from pristine LNR9. The inset in **a** shows the superstructure peaks from in-plane ordering between Li and TM within TM layer, which fades away after cycling.

Supplementary Table 2 | *Ex situ* sample descriptions and XRD measurement conditions

Sample description	Cycling condition	XRD beamline	X-ray wavelength (Å)
OL (LNR0) pristine	N/A	APS 11-BM-B	0.459073
OL (LNR0) after 1 cycle	1 cycle of C/20 2.5–4.7 V w/ CV hold	SSRL 2-1	0.729760
OL (LNR0) after ≈100 cycles	1 cycle of C/20 2.5–4.7 V w/ CV hold 100 cycles of C/2 2.5–4.7V w/ charge-only CV hold 4 cycles of C/20 2.5–4.7 V w/ CV hold	APS 11-BM-B	0.459073
LNR3 pristine	N/A	SSRL 2-1	0.729760
LNR5 pristine	N/A	SSRL 2-1	0.729760
DL(5) LNR5 after 1 cycle	1 cycle of C/20 2.5–4.7 V w/ CV hold	APS 11-BM-B	0.459738
DL(5) LNR5 after 5 cycles	5 cycles of C/20 2.5–4.7 V w/ CV hold	APS 11-BM-B	0.459744
DL(5) LNR5 after ≈100 cycles	1 cycle of C/20 2.5–4.7 V w/ CV hold 100 cycles of C/2 2.5–4.7V w/ charge-only CV hold 4 cycles of C/20 2.5–4.7 V w/ CV hold	APS 11-BM-B	0.459073
LNR9 pristine	N/A	APS 11-BM-B	0.459073
LNR9 after 1st charge	1 charge of C/20 to 4.7 V w/ CV hold	SSRL 2-1	0.729760
DL(9) LNR9 after 1 cycle	1 cycle of C/20 2.5–4.7 V w/ CV hold	APS 11-BM-B	0.459738
DL(9) LNR9 after 2 cycles	2 cycles of C/20 2.5–4.7 V w/ CV hold	APS 11-BM-B	0.459738
DL(9) LNR9 after 5 cycles	5 cycles of C/20 2.5–4.7 V w/ CV hold	APS 11-BM-B	0.459738
DL(9) LNR9 after ≈50 cycles	1 cycle of C/20 2.5–4.7 V w/ CV hold 50 cycles of C/2 2.5–4.7V w/ charge-only CV hold 4 cycles of C/20 2.5–4.7 V w/ CV hold	APS 11-BM-B	0.459073
DL(9) LNR9 after ≈100 cycles	1 cycle of C/20 2.5–4.7 V w/ CV hold 100 cycles of C/2 2.5–4.7V w/ charge-only CV hold 4 cycles of C/20 2.5–4.7 V w/ CV hold	APS 11-BM-B	0.459073
DL(9) LNR9 after ≈100 cycles (4.7 → 4.3 V)	1 cycle of C/20 2.5–4.7 V w/ CV hold 4 cycles of C/10 2.5–4.7 V w/ CV hold 97 cycles of C/10 2.5–4.3V w/ CV hold	APS 11-BM-B	0.459738

1C = 200 mA g^{-1}. Charge CV hold limit: C/50. Discharge CV hold limit: C/500.

Supplementary Table 3 | Rietveld refinement results for *ex situ* XRD measurements

Space group: $R\bar{3}m$ (166)

Sample description	**Lattice parameters**	**3*a* Wyckoff position**		**3*b* Wyckoff position**		**6*c* Wyckoff position**	
		coordinate	**occupancy**	**coordinate**	**occupancy**	**coordinate**	**occupancy**
OL (LNR0) pristine	a/Å: 2.877614(12) c/Å: 14.21421(12) V/Å^3: 101.934(1)	0, 0, 0	Ni: 0.845(3) Mn: 0.0991(3) Li: 0.056(3)	0, 0, 1/2	Li: 0.9530(8) Ni: 0.0470(8)	0, 0, 0.25918(6)	O: 1
OL (LNR0) after 1 cycle	a/Å: 2.87770(3) c/Å: 14.2164(3) V/Å^3: 101.955(3)	0, 0, 0	Ni: 0.842(3) Mn: 0.1004(3) Li: 0.061(2)	0, 0, 1/2	Li: 0.934(4) Ni: 0.066(4)	0, 0, 0.26033(12)	O: 1
OL (LNR0) after ≈100 cycles	a/Å: 2.883309(18) c/Å: 14.23958(18) V/Å^3: 102.520(2)	0, 0, 0	Ni: 0.852(2) Mn: 0.10117(17) Li: 0.0583(14)	0, 0, 1/2	Li: 0.930(2) Ni: 0.070(2)	0, 0, 0.25920(7)	O: 1
LNR3 pristine	a/Å: 2.87264(3) c/Å: 14.1923(2) V/Å^3: 101.425(2)	0, 0, 0	Ni: 0.817(4) Mn: 0.0981(5) Li: 0.085(5)	0, 0, 1/2	Li: 0.9346(13) Ni: 0.0654(13)	0, 0, 0.25878(10)	O: 1
LNR5 pristine	a/Å: 2.86666(3) c/Å: 14.1784(2) V/Å^3: 100.905(2)	0, 0, 0	Ni: 0.795(4) Mn: 0.0950(4) Li: 0.110(5)	0, 0, 1/2	Li: 0.9400(12) Ni: 0.0600(12)	0, 0, 0.25906(10)	O: 1
DL(5) LNR5 after 1 cycle	a/Å: 2.87515(2) c/Å: 14.2118(2) V/Å^3: 101.742(2)	0, 0, 0	Ni: 0.814(2) Mn: 0.0986(3) Li: 0.087(3)	0, 0, 1/2	Li: 0.9270(7) Ni: 0.0730(7)	0, 0, 0.25922(6)	O: 1
DL(5) LNR5 after 5 cycles	a/Å: 2.87885(4) c/Å: 14.2254(5) V/Å^3: 102.102(5)	0, 0, 0	Ni: 0.813(3) Mn: 0.1007(2) Li: 0.0939(19)	0, 0, 1/2	Li: 0.898(3) Ni: 0.102(3)	0, 0, 0.25907(11)	O: 1
DL(5) LNR5 after ≈100 cycles	a/Å: 2.88937(4) c/Å: 14.2635(4) V/Å^3: 103.124(4)	0, 0, 0	Ni: 0.7829(18) Mn: 0.10217(16) Li: 0.1366(11)	0, 0, 1/2	Li: 0.8418(19) Ni: 0.1582(19)	0, 0, 0.25902(8)	O: 1
LNR9 pristine	a/Å: 2.85464(3) c/Å: 14.1576(3) V/Å^3: 99.913(3)	0, 0, 0	Ni: 0.775(4) Mn: 0.0894(4) Li: 0.136(4)	0, 0, 1/2	Li: 0.9698(11) Ni: 0.0302(11)	0, 0, 0.26002(8)	O: 1
LNR9 after 1st charge*	a/Å: 2.83033(8) c/Å: 14.2200(7) V/Å^3: 98.651(7)	0, 0, 0	Ni: 0.7658(14) Mn: 0.0981 Li: 0	0, 0, 1/2	Li: 0 Ni: 0.1169(14)	0, 0, 0.26220(14)	O: 1
DL(9) LNR9 after 1 cycle	a/Å: 2.87675(4) c/Å: 14.2335(5) V/Å^3: 102.011(4)	0, 0, 0	Ni: 0.766(3) Mn: 0.0981(3) Li: 0.136(4)	0, 0, 1/2	Li: 0.8831(10) Ni: 0.1169(10)	0, 0, 0.25879(8)	O: 1
DL(9) LNR9 after 2 cycles	a/Å: 2.87476(4) c/Å: 14.2240(5) V/Å^3: 101.802(5)	0, 0, 0	Ni: 0.779(3) Mn: 0.0998(4) Li: 0.121(4)	0, 0, 1/2	Li: 0.8810(9) Ni: 0.1190(9)	0, 0, 0.26143(8)	O: 1
DL(9) LNR9 after 5 cycles	a/Å: 2.87923(3) c/Å: 14.2546(3) V/Å^3: 102.338(3)	0, 0, 0	Ni: 0.7878(16) Mn: 0.10099(14) Li: 0.1210(10)	0, 0, 1/2	Li: 0.8691(17) Ni: 0.1309(17)	0, 0, 0.25819(7)	O: 1
DL(9) LNR9 after ≈50 cycles	a/Å: 2.89344(4) c/Å: 14.2811(4) V/Å^3: 103.543(4)	0, 0, 0	Ni: 0.760(2) Mn: 0.10270(19) Li: 0.1644(13)	0, 0, 1/2	Li: 0.809(2) Ni: 0.191(2)	0, 0, 0.25783(9)	O: 1
DL(9) LNR9 after ≈100 cycles	a/Å: 2.89590(5) c/Å: 14.2433(6) V/Å^3: 103.445(6)	0, 0, 0	Ni: 0.7289(15) Mn: 0.10145(13) Li: 0.1842(9)	0, 0, 1/2	Li: 0.8013(16) Ni: 0.1987(16)	0, 0, 0.25750(7)	O: 1
DL(9) LNR9 after ≈100 cycles (4.7 → 4.3 V)	a/Å: 2.89211(3) c/Å: 14.3039(4) V/Å^3: 103.613(3)	0, 0, 0	Ni: 0.7507(14) Mn: 0.10059(12) Li: 0.1547(8)	0, 0, 1/2	Li: 0.8394(15) Ni: 0.1606(15)	0, 0, 0.25803(6)	O: 1

Total Ni:Mn fixed as 9:1. All sites assumed to be fully occupied.

* Assumed no Li remaining. Ni and Mn content per cell fixed to be same as in sample ‘LNR9 after 1 cycle’.

3.3. Ni XANES.

XANES at the Ni K-edge (Supplementary Fig. 8) is used to deduce the average oxidation state of Ni, which can be used to infer the composition of the electrochemically-active phase of cathode based on overall neutrality of oxidation state. Since XANES is element-selective, inactive phases with no Ni will not influence the signal. Except Ni, all other elements involved have a fixed oxidation state: Li^{1+}, O^{2-}, and Mn^{4+}. Oxygen is assumed to have 2- oxidation state since all samples were fully discharged to 2.5 V with a long CV hold, and we do not expect oxidized oxygen to be possible at such a low potential. Even though Mn can be redox-active, it will have a fixed 4+ oxidation state in the Ni-rich systems considered here. This is because the energy bands of Mn redox couples ($Mn^{3+/2+}$ and $Mn^{4+/3+}$) have much higher energies and do not overlap with Ni redox couples ($Ni^{3+/2+}$ and $Ni^{4+/3+}$)[1,80]. In particles with Ni having greater than 2+ oxidation state, Mn will be at 4+ state.

A higher oxidation state will cause a shift of XANES towards higher energy. It can be seen that pristine LNRi shifts to a higher energy with a larger i (Supplementary Fig. 8a), LNR0 changes little after cycling (Supplementary Fig. 8b), and LNR9 shifts to a lower energy after its first cycle (Supplementary Fig. 8c).

For Ni six-fold coordinated by O in NiO_6 octahedra as in layered oxide, the white-line energy (energy where the normalized absorbance μ is maximum) from K-edge XANES varies linearly with the nominal average oxidation state. Therefore, white-line energies from two materials with known Ni oxidation states can be used for in-/extra-polation references. However, it is challenging to obtain such good reference materials from external suppliers because of the uncertainty in the true composition and the instability of high-valence Ni compounds. Therefore, we selected two as-synthesized samples which we have high confidence in the true compositions of the electrochemically-active phase as the references. Pristine LNR0 was found to have near ideal stoichiometric composition using both ICP+NMR and XRD techniques, and therefore it is taken to be $Li_{1.000}Ni_{0.900}Mn_{0.100}O_2$ and used as $Ni^{2.89+}$ reference. Different batches of pristine LNR9 were tested by ICP+NMR technique and consistently yielded a composition close to $Li_{1.088}Ni_{0.821}Mn_{0.091}O_2$ (within 1% deviation). Therefore, LNR9 is taken with this composition and used as a $Ni^{3.10+}$ reference. The oxidation states fitted using these references are shown in Supplementary Table 4 (for *ex situ* samples) and in Fig. 1b (for *operando* measurement). The calculated Ni oxidation states from *operando* data having maximum close to the expected number of 4.0+ suggests the validity of the references and the white-line energy method[81].

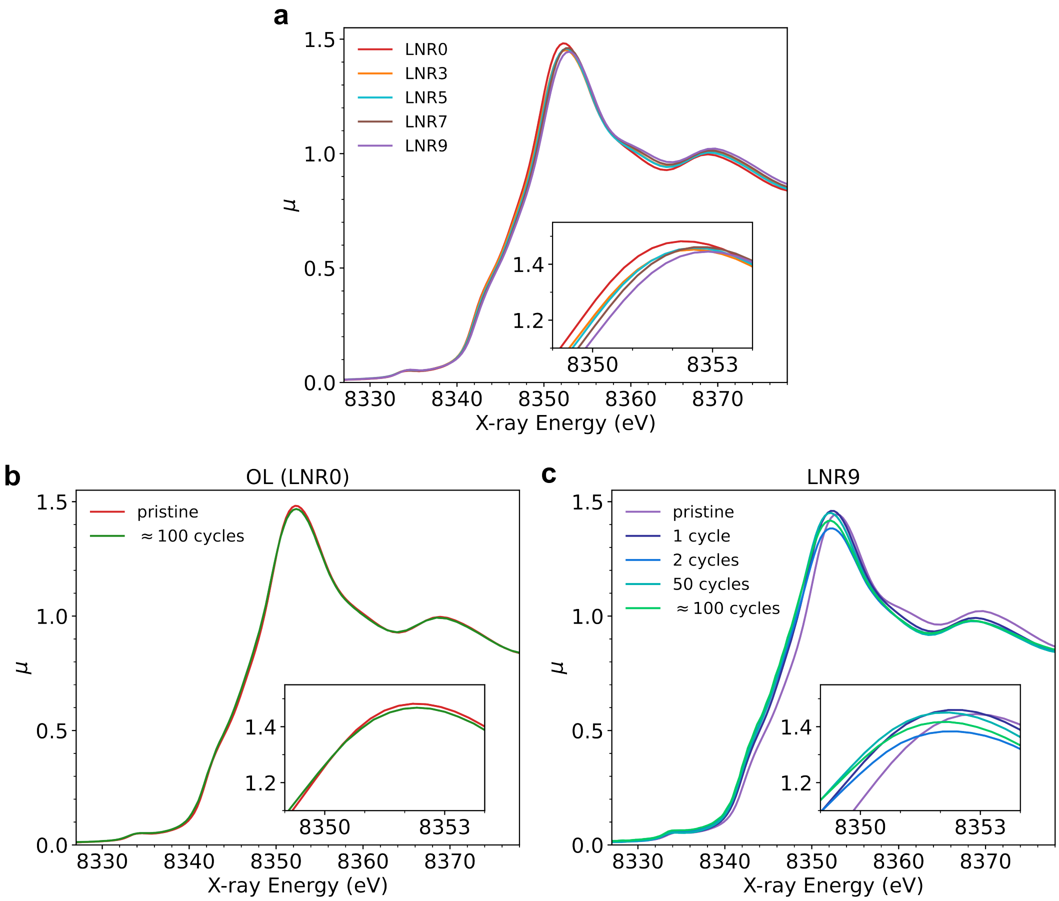

Supplementary Fig. 8 | a–c, Ni K-edge XANES spectra for LNR*i* with different levels of Li-excess (**a**), pristine and cycled OL (LNR0) (**b**), and pristine LNR9 and cycled DL(9) (**c**).

Supplementary Table 4 | *Ex situ* Ni K-edge XANES spectra white-line energies and the calculated oxidation states of Ni

Sample description	Ni K-edge white-line energy (eV)	Calculated average Ni valence state
OL (LNR0) pristine*	8352.29	+2.89*
OL (LNR0) after ≈100 cycles	8352.30	+2.90
LNR3 pristine	8352.51	+2.97
LNR5 pristine	8352.59	+3.00
LNR7 pristine	8352.70	+3.04
LNR9 pristine**	8352.87	+3.10**
DL(9) LNR after 1 cycle	8352.36	+2.92
DL(9) LNR after 2 cycles	8352.27	+2.88
DL(9) LNR after ≈50 cycles	8352.11	+2.83
DL(9) LNR after ≈100 cycles	8352.10	+2.82

* Reference for valence state fitting.

* Assumed to be stoichiometric $Li_{1.000}Ni_{0.900}Mn_{0.100}O_2$.

** Reference for valence state fitting.

** Assumed to be $Li_{1.088}Ni_{0.821}Mn_{0.091}O_2$ with Li content from ICP+NMR.

3.4. Summary of composition analysis results.

By deploying measurements based on different principles (ICP: total chemical analysis, NMR: local magnetic environment, XRD: diffraction, XANES: electronic structure), we determined chemical compositions for the electrochemically-active phases from the following independent approaches: coupled ICP+NMR, XRD refinement, and XANES analysis (Supplementary Table 5). The values obtained for each sample with different approaches agree well with each other.

Supplementary Table 5 | Compositions determined by different approaches and the chemical formula used for converting capacity to composition

Sample description	Composition			Average composition*** (used in electrochemical conversion)
	from ICP+NMR	from XRD**	from XANES**	
OL (LNR0) pristine	$Li_{0.992}Ni_{0.920}Mn_{0.088}O_2$	$Li_{1.009}Ni_{0.892}Mn_{0.099}O_2$	N/A (reference) (assumed composition: $Li_{1.000}Ni_{0.900}Mn_{0.100}O_2$)	$Li_{1.000}Ni_{0.900}Mn_{0.100}O_2\text{-}B_{0.010}$
OL (LNR0) after 1 cycle	N/A	$Li_{0.996}Ni_{0.904}Mn_{0.100}O_2$	N/A	$Li_{0.996}Ni_{0.904}Mn_{0.100}O_2\text{-}B_{0.010}$
OL (LNR0) after ≈100 cycles	N/A	$Li_{0.988}Ni_{0.911}Mn_{0.101}O_2$	$Li_{1.003}Ni_{0.897}Mn_{0.100}O_2$	$Li_{0.996}Ni_{0.904}Mn_{0.100}O_2\text{-}B_{0.010}$
LNR3 pristine	N/A	$Li_{1.019}Ni_{0.883}Mn_{0.098}O_2$	$Li_{1.035}Ni_{0.869}Mn_{0.097}O_2$	$Li_{1.027}Ni_{0.876}Mn_{0.097}O_2\text{-}B_{0.010}$
LNR5 pristine	N/A	$Li_{1.050}Ni_{0.855}Mn_{0.095}O_2$	$Li_{1.047}Ni_{0.858}Mn_{0.095}O_2$	$Li_{1.048}Ni_{0.856}Mn_{0.095}O_2\text{-}B_{0.011}$
DL(5) LNR5 after 1 cycle	N/A	$Li_{1.014}Ni_{0.887}Mn_{0.099}O_2$	N/A	$Li_{1.014}Ni_{0.887}Mn_{0.099}O_2\text{-}B_{0.011}$
DL(5) LNR5 after 5 cycles	N/A	$Li_{0.992}Ni_{0.907}Mn_{0.101}O_2$	N/A	$Li_{0.992}Ni_{0.907}Mn_{0.101}O_2\text{-}B_{0.011}$
DL(5) LNR5 after ≈100 cycles	N/A	$Li_{0.978}Ni_{0.920}Mn_{0.102}O_2$	N/A	$Li_{0.978}Ni_{0.920}Mn_{0.102}O_2\text{-}B_{0.011}$
LNR7 pristine	N/A	N/A	$Li_{1.063}Ni_{0.843}Mn_{0.094}O_2$	$Li_{1.063}Ni_{0.843}Mn_{0.094}O_2\text{-}B_{0.011}$
LNR9 pristine*	$Li_{1.088}Ni_{0.814}Mn_{0.099}O_2$	$Li_{1.106}Ni_{0.805}Mn_{0.089}O_2$	N/A (reference) (assumed composition: $Li_{1.088}Ni_{0.821}Mn_{0.091}O_2$)	$Li_{1.088}Ni_{0.821}Mn_{0.091}O_2\text{-}B_{0.011}$
DL(9) LNR after 1 cycle	$Li_{0.992}Ni_{0.895}Mn_{0.111}O_2$	$Li_{1.019}Ni_{0.883}Mn_{0.098}O_2$	$Li_{1.012}Ni_{0.889}Mn_{0.099}O_2$	$Li_{1.008}Ni_{0.893}Mn_{0.099}O_2\text{-}B_{0.012}$
DL(9) LNR after 2 cycles	$Li_{1.009}Ni_{0.883}Mn_{0.108}O_2$	$Li_{1.002}Ni_{0.898}Mn_{0.100}O_2$	$Li_{0.997}Ni_{0.903}Mn_{0.100}O_2$	$Li_{1.003}Ni_{0.898}Mn_{0.100}O_2\text{-}B_{0.012}$
DL(9) LNR after 5 cycles	$Li_{1.020}Ni_{0.881}Mn_{0.099}O_2$	$Li_{0.990}Ni_{0.909}Mn_{0.101}O_2$	N/A	$Li_{1.005}Ni_{0.896}Mn_{0.100}O_2\text{-}B_{0.012}$
DL(9) LNR after ≈50 cycles	N/A	$Li_{0.973}Ni_{0.924}Mn_{0.103}O_2$	$Li_{0.971}Ni_{0.926}Mn_{0.103}O_2$	$Li_{0.972}Ni_{0.925}Mn_{0.103}O_2\text{-}B_{0.012}$
DL(9) LNR after ≈100 cycles	N/A	$Li_{0.985}Ni_{0.913}Mn_{0.101}O_2$	$Li_{0.969}Ni_{0.928}Mn_{0.103}O_2$	$Li_{0.977}Ni_{0.920}Mn_{0.102}O_2\text{-}B_{0.012}$
DL(9) LNR9 after ≈100 cycles (4.7 → 4.3 V)	$Li_{1.019}Ni_{0.882}Mn_{0.099}O_2$	$Li_{0.994}Ni_{0.905}Mn_{0.101}O_2$	N/A	$Li_{1.006}Ni_{0.894}Mn_{0.099}O_2\text{-}B_{0.012}$

* Consistent Li content (± 0.01 standard deviation) were obtained from multiple batches of this sample using coupled ICP+NMR quantification.
* Average composition was set to ICP+NMR result.
** Ni:Mn atomic ratio fixed to 9:1.
*** B amount is estimated (based on nominal B:TM ratio in precursor), not measured.

In all associated analyses, we assumed the absence of crystallographic oxygen vacancies. Although it has been proposed that persistent oxygen vacancies can be present in a cycled Mn-rich cathode[35], we do not believe the evidences suggest this to be the case for these Ni-rich systems. The presence of nanoscale oxygen gas pockets inside cathode particles[29,30] is possible, but we cannot verify it at this stage since these vacancy pockets have no impact on the measurements we did here. Another assumption we had is that samples are in the fully discharged (lithiated) state with no cation site vacancy. We prepared all discharged samples used for composition analyses by lithiating at 2.5 V (*vs.* Li/Li^+) with prolonged CV holds to make sure this assumption is met as closely as possible.

We note here that if the above two assumptions were invalid, the three methods would yield conflicting results. If oxygen vacancies were indeed present ($\mathrm{Li}_{1+\gamma}\mathrm{TM}_{1\text{-}\gamma}\mathrm{O}_{2\text{-}v}$) and we erroneously assumed $v = 0$, we would still accurately estimate the amount of TM per unit formula from ICP+NMR and XRD, but we would overestimate TM per formula unit from XANES. If the material could not fully lithiate and was left behind with Li vacancies ($\mathrm{Li}_{1+\gamma\text{-}v}\mathrm{TM}_{1\text{-}\gamma}\mathrm{O}_2$), by assuming $v = 0$, we would overestimate TM per formula unit from ICP+NMR, underestimate TM per formula unit from XANES, but TM per formula unit estimated from XRD remain relatively unaffected. Since consistent compositions are obtained in Supplementary Table 5, we conclude that it is unlikely that substantial bulk oxygen vacancies or Li vacancies are present in this material system. However, we acknowledge that we could not rule out the possibility of the existence of a small fraction (≈1%) of overall oxygen vacancy or Li vacancy, either persistent in the bulk or localized at the surface, which is beyond the accuracy and sensitivity limit of these methods.

3.5. Extra note: Specific capacity and Li count in cell testing and *operando* measurements.

For some figures showing the electrochemical or *operando* measurement results, we plotted the number of Li remaining in the electrochemically-active phase of cathode ($\mathrm{Li}_x\mathrm{TM}_{1\text{-}x_0}\mathrm{O}_2$). The values of x were derived directly from the nominally measured capacity from cell cycling according to $\Delta x = (Q \cdot F.W.)/(n \cdot F)$ where Q is the specific capacity based on direct CAM mass, $F.W.$ is the adjusted formula weight for the electrochemically-active phase of cathode, F is the Faraday constant, and the electron transfer number $n = 1$ for Li^+. The starting value of x_{Li} in the discharged state before *operando* measurement is taken from the composition determined from *ex situ* sample having a similar condition (Supplementary Table 5).

The adjusted formula weight for the electrochemically-active phase of cathode ($F.W.$) is calculated based on the column 'average composition' in Supplementary Table 5. The pristine electrodes were made from slurries containing 80 wt% CAM. For regular cell tests other than *operando* measurement, the reported specific capacities are always based on the CAM mass from the pristine electrodes. For *operando* measurement of non-pristine state samples, the electrodes were harvested from coin cells to make the *operando* pouch cells. However, because DL(i) has a different chemical composition of the electrochemically-active phase than that of its predecessor LNRi, the CAM weight fraction in electrode is expected to be slightly lower for DL(i). To have a more accurate estimation on CAM percentage in electrode, conversions are done by assuming CAM can be represented by the 'average composition' in Supplementary Table 5 and that the total TM in the electrode remain unchanged from LNRi to DL(i). Total masses of the inactive electrode ingredients (C and PVDF) in electrodes are assumed unchanged as well. The *operando* specific capacities we report are calculated using these corrected CAM masses for harvested DL(i) electrodes.

We note that in the calculation of $F.W.$, inactive components within CAM are either not counted ((*e.g.* $\mathrm{Li}_2\mathrm{CO}_3$)) or under-counted (B is used to represent the B-based surface coating expected to have composition between LiBO_2 and $\mathrm{B}_2\mathrm{O}_3$[23,25,26,82]). Therefore, $F.W.$ used is a preservative lower-bound. This factor would cause an underestimate of the calculated Δx_{Li}. Additionally, we suspect the existence of some small amount of 'corrosion' current (*i.e.* current not from the lithiation or delithiation of CAM, *e.g.*, corrosion of the metallic cell components or electrolyte degradation), particularly at high potentials during the early cycles (during which we have observed some cells displaying capacities higher than theoretically predicted in our lab tests). This factor will cause an overestimation of the calculated Δx_{Li}. Overall, it is inconclusive how our calculated Δx_{Li} compares to the true value. However, both errors (due to formula weight uncertainty and corrosion current) are small, and we expect the calculated Δx_{Li} to be very close to the true value, with a deviation not exceeding 5%.

4. Supplementary Discussion: Electrochemical Activation of LNR to DL

4.1. Oxygen oxidation and oxygen release.

The oxidation of oxygen anions is believed to be the trigger for the electrochemical activation of LNR into DL. Supplementary Fig. 9 shows the data (voltage profile and absorption spectra) collected from *operando* Ni K-edge XANES measurement during the 1st charge of LNR9, whose analysis result is presented in Fig. 1b. It is clear from Supplementary Fig. 9a that the XANES spectra shift in the direction of higher X-ray energy at the beginning of delithiation, corresponding to the oxidation of Ni (*i.e.*, the depopulation of hybridized Ni 3*d*–O 2*p* band). However, that shift stopped towards the end, at which point the oxidation of oxygen anions (*i.e.*, the depopulation of states with predominantly O 2*p* character) charge-compensates the removal of Li$^+$ [18,27,28,31,66–73].

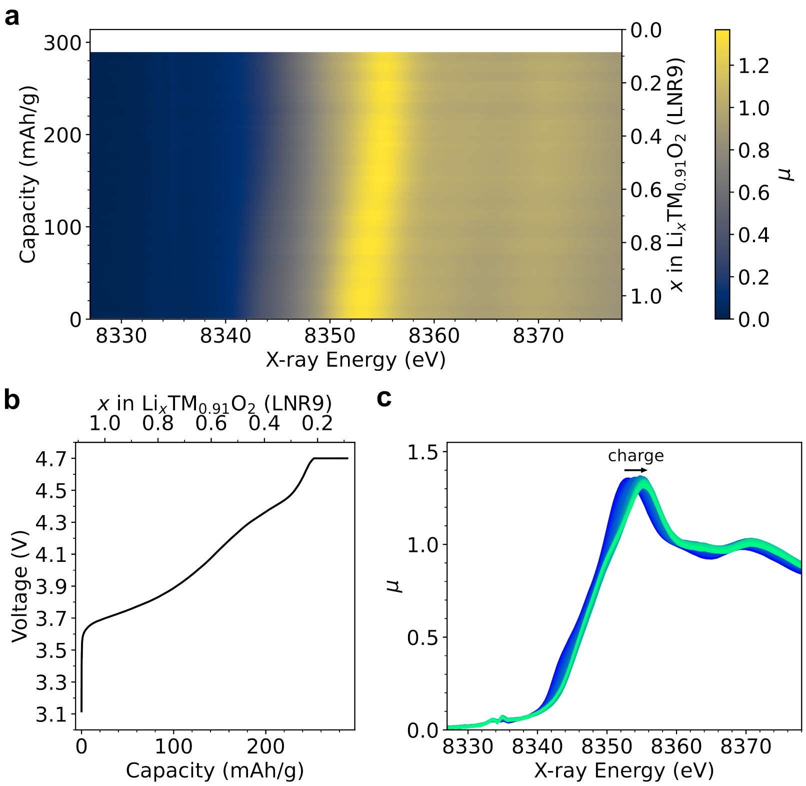

Supplementary Fig. 9 | Ni K-edge *operando* XANES data during the first charge of LNR9. **a**, Intensity map of XANES spectra against capacity / composition of the electrochemically-active phase of cathode. **b**, Associated voltage profile during *operando* measurement. **c**, XANES spectra collected. The analyzed result of these data is shown in Fig. 1b.

The relithiation during the 1st discharge of LNR9 is charge-compensated almost solely by Ni reduction (Fig. 1b), which is supported by the numerical results of Coulombic mismatch (Fig. 1a), chemical analysis (Supplementary Information section 3.1), and *ex situ* XANES measurement (Supplementary Information section 3.3). Therefore, certain process of chemical disproportion reaction is expected to happen for the oxidized oxygen species, converting some back to O^{2-} ions in the cathode lattice and some to O_2 gas.

This release of O_2 gas from the cathode lattice is supported by the *operando* DEMS measurement during 1st charge of LNR9 (Supplementary Fig. 10a,b). As elaborated in the discussion of the main article, this caused a structural evolution of LNR9 to DL(9). For comparison, *operando* DEMS result with the same setup on a future charge half-cycle of activated DL(9) is presented in Supplementary Fig. 10a,c. No significant O_2 or CO_2 release was detected for DL(9) up to 4.7 V UCV. This confirms that the O_2 DEMS signal observed during the activation charge of LNR9 came from lattice oxygen release rather than electrolyte decomposition.

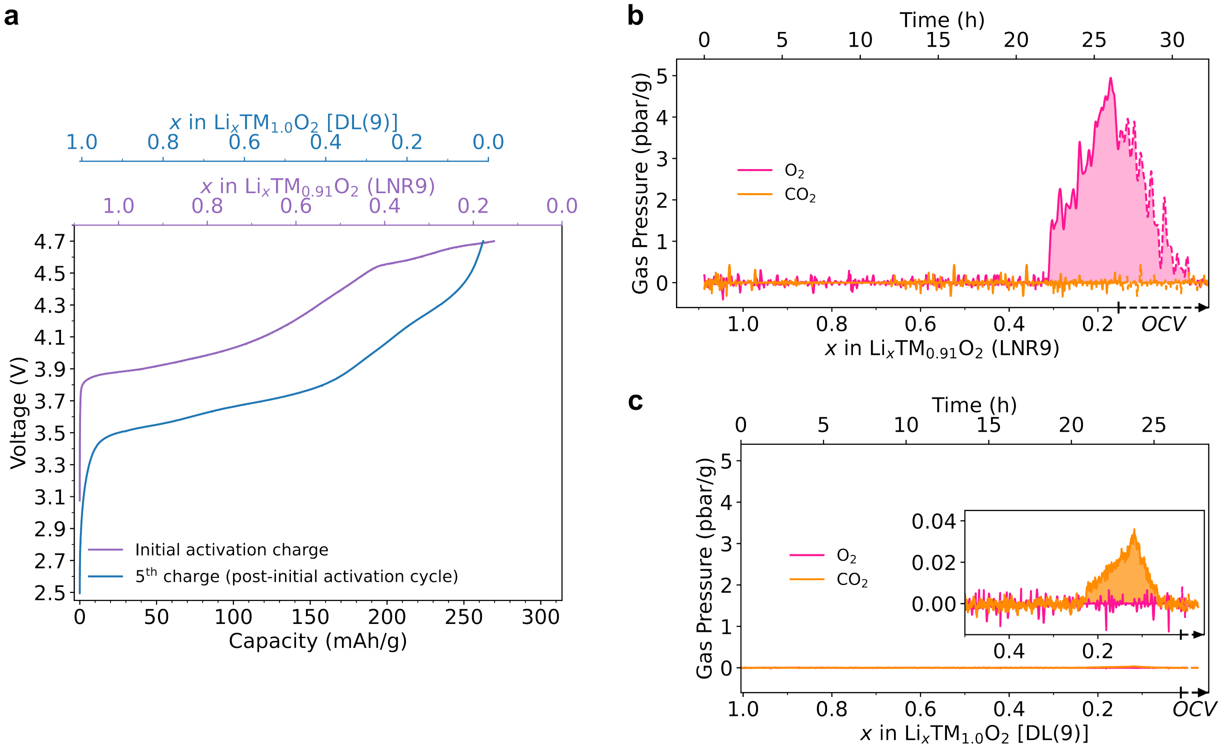

Supplementary Fig. 10 | **a**, Voltage profiles of the initial activation charge of LNR9 and 5th charge of DL(9) post initial activation obtained during *operando* DEMS measurements. Both specific capacities are based on CAM mass of pristine LNR9 in electrode. The estimated Li content per formula unit of LNR9 and DL(9) are also displayed. **b**, The detected O_2 and CO_2 gas pressures (normalized by pristine LNR9 CAM mass in electrode) from DEMS measurement during initial activation charge of LNR9. This is a duplicate of Fig. 1c. **c**, Detected O_2 and CO_2 from DEMS measurement during charge of DL(9) (5th charge after the initial activation cycle). During *operando* DEMS for both cells: 10 mA g^{-1} CC charge to 4.7 V without CV hold. Pre-cycling for the DL(9) electrode (in a sealed coin half-cell): 10 mA g^{-1} CC charge to 4.7 V without CV hold, 10 mA g^{-1} CC discharge to 2.5 V with CV hold until discharge capacity matches charge capacity, repeated for a total of 5 cycles.

4.2. Lattice parameter evolution during the electrochemical activation cycle of LNR.

Supplementary Figs. 11 and 12 show the *operando* XRD results and evolution of lattice parameters during the 1st charge of LNR5 and LNR9, respectively. It is evident that changes in the **c** lattice parameter remain small during the activation cycle where LNR evolves to DL. The small **c**-strain during activation probably has some differences in its origin compared to stabilized DL. Though the exact reason is not clear, active oxygen oxidation or reduction seem to have a strong impact on the behavior of **c** during (de)lithiation, and small **c**-strains have been observed in many material systems during O-redox[21,79,83]. Similar observations are made here for delithiated LNR5 and LNR9: changes in **c** remain small in the Li-scarce states when active oxygen oxidation is taking place.

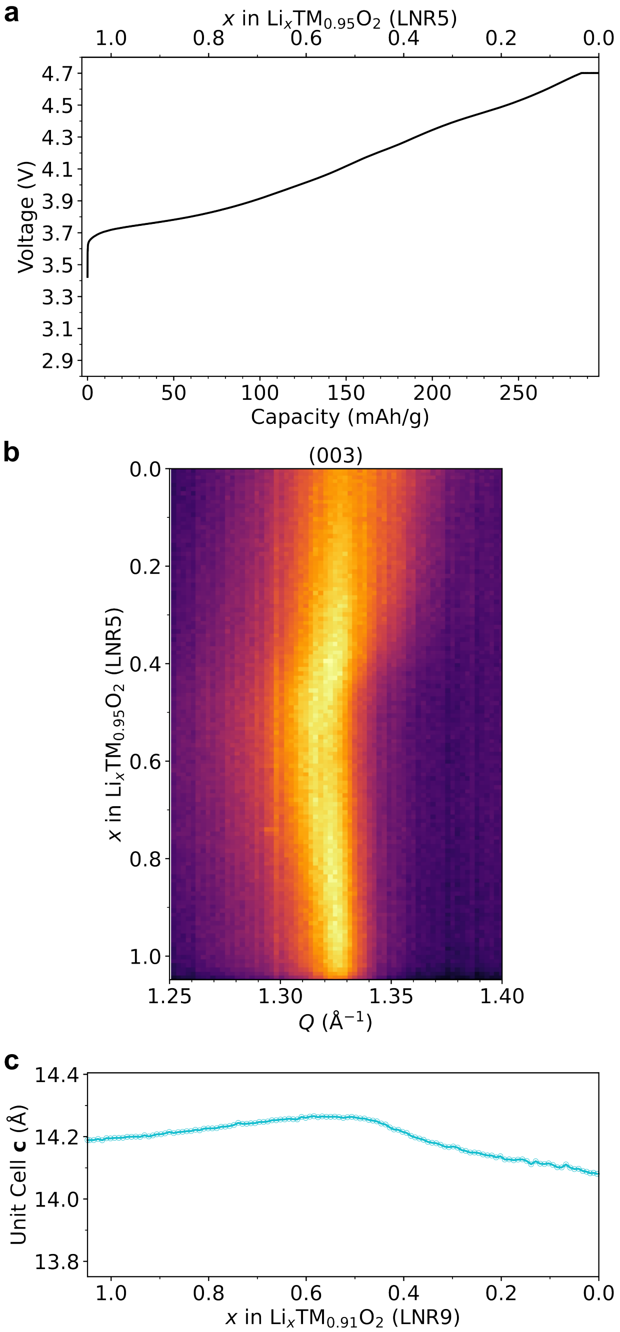

Supplementary Fig. 11 | **a**–**c**, Voltage profile (**a**), evolution of (003) diffraction peak (**b**), changes in **c** lattice parameter (**c**) from *operando* XRD during the activation of LNR5 where it evolves to DL(5) (*i.e.*, 1st charge of LNR5). X-ray source: Mo K_α.

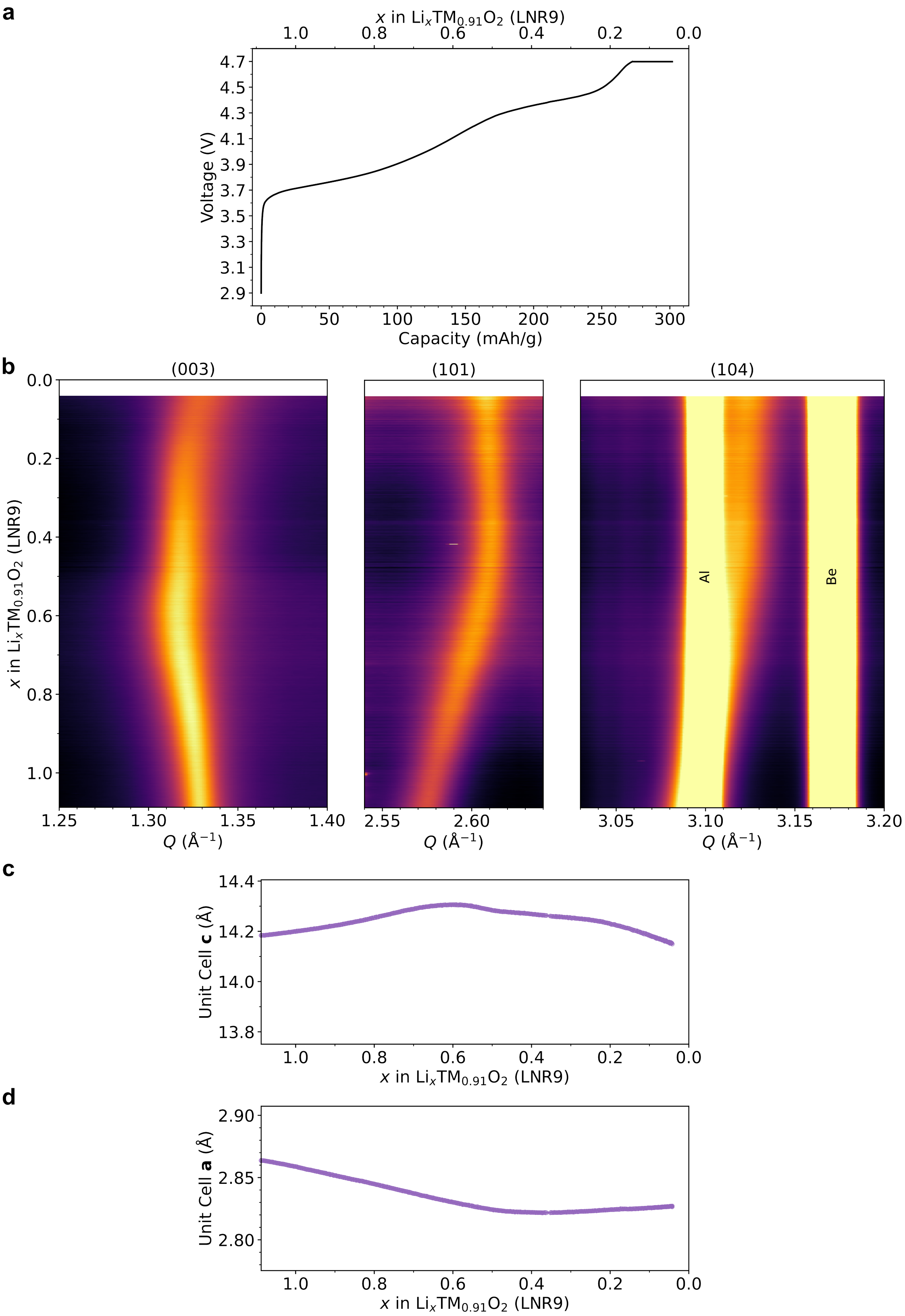

Supplementary Fig. 12 | **a**–**d**, Voltage profile (**a**), evolution of (003), (101), and (104) diffraction peaks (**b**), changes in **c** lattice parameter (**c**), and changes in **a** lattice parameter (**d**) from *operando* XRD during the activation of LNR9 where it evolves to DL(9) (*i.e.*, 1st charge of LNR9). X-ray wavelength: 0.97625 Å.

4.3. Stability of DL post activation.

We verify the rigidity of the microstructure after LNR activates to DL, as well as the chemical and structural stability of DL post activation.

Microstructural rigidity is verified by cross-sectional SEM. As shown in Supplementary Fig. 13, the interior of the secondary particle remains intact and compact after pristine LNR9 is activated into DL(9), despite the release of O_2. The activation does not result in the generation of extended cracks. No apparent difference in shape or size of the secondary particles, primary particles, or porosity within the secondary particles is observed between LNR9 and DL(9).

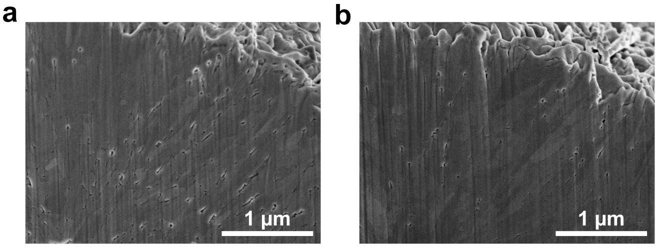

Supplementary Fig. 13 | **a**,**b**, Representative FIB cross-section images of pristine LNR9 (**a**) and DL(9) (LNR9 after 1 cycle) (**b**).

Post-activation stability of DL is evaluated by subjecting samples to further aggressive electrochemical cycling with 4.7 V UCV (same as activation).

The gas release behavior is tested using *operando* DEMS on activated DL(9) (Supplementary Fig. 10a,c). Negligible O_2 and CO_2 gases are detected during the charging of activated DL(9) to 4.7 V (at least two orders of magnitude smaller than O_2 released in the first activation cycle). This confirms bulk structural evolution is not a chronic process after initial activation cycles, and the activation process is quickly finished. Some trace CO_2 signals can be identified in DL(9) after being deeply delithiated beyond $x_{\mathrm{Li}} < 0.25$ (Supplementary Fig. 10c inset), similar to conventional stoichiometric lithium TM oxide and the responsible process is probably confined to the particle surface[33,34,84].

The results of composition and structure analyses (Supplementary Information section 3) for samples under different numbers of 4.7 UCV cycles are summarized in Supplementary Fig. 14. LNR0 has no significant change in composition or structure even after 100 cycles, and it remains ordered. This conclusion matches the observation of a stable lineshape in the ^{7}Li NMR data (Supplementary Fig. 4a). For LNR5 and LNR9, large changes to the composition and structure of their electrochemically-active phases happen after the first cycle, and we denote the activated materials DL(5) and DL(9), respectively. Relatively small changes are seen in DL(5) and DL(9) with further 4.7 V UCV cycles. With a small number of 4.7 V UCV cycles ($\leq$5), both DL(5) and DL(9) have close-to-stoichiometric compositions as OL. The increased $\mathrm{TM}_{\mathrm{Li}}$ concentration in DL(i) correlates positively with i (*i.e.* pristine Li-excess in LNRi). For the $\mathrm{TM}_{\mathrm{TM}}$ concentration, the difference between pristine LNRi and activated DL(i) is small.

However, if such aggressive 4.7 V UCV cycling continued extensively for 50 or 100 cycles, some changes can be noticed in DL(5) and DL(9). The results suggest a decrease in the overall Li stoichiometry of the electrochemically-active phase and an increase in structural disorder. It is possible these are the manifestation of accumulated surface degradation. DEMS result in Supplementary Fig. 10c show tiny CO_2 formation at high voltage. These CO_2 can likely be traced to minor oxygen release at the cathode particle surface, which is well-reported in over-charged conventional cathodes, especially if they are Ni-rich[1,33,34,84,85]. The origin of this long-term degradation can be complicated. One possibility is the continued participation of minor oxygen-redox even if DL is no longer Li-excess. This deviation from the idealized scenario in Supplementary Fig. 3 is not unexpected since energy overlap between $\mathrm{Ni}^{4+}/\mathrm{Ni}^{3+}$ couple and O $2p$ band is known[1], and the sequence of redox mechanisms is structure- and kinetics-dependent[75]. Such low levels of oxidized oxygen may not be able to drive bulk cathode evolution, but they may gradually change the surface layer. Surface layer with a rock salt-type crystal structure is commonly seen in degraded Ni-rich cathodes[22]. If the lattice of the surface rock salt is coherent to the bulk cathode lattice, no extra diffraction peak will appear but the outcome of Rietveld refinement will be affected. After 50 or 100 cycles at 4.7 V UCV, it is reasonable that surface rock salt layers form on DL(5) and DL(9). These surface layers will be Li-poor and highly disordered, even if the bulk of DL(5) and DL(9) cathodes do not change.

An effective way to minimize surface degradation is to avoid high potentials[45,86,87], and for the activated DL, there is little extra capacity from 4.3 V to 4.7 V. Supplementary Fig. 15 shows that having an extra ≈100 cycles with a 4.3 V UCV (besides five cycles with a 4.7 V UCV) does not cause a significant difference in the composition of the electrochemically-active phase and structure disorder. Comparing Supplementary Figs. 14 and 15, it can be seen that the impact of high-potential surface degradation to DL(9) is much less severe if UCV is limited to 4.3 V after activation. This finding suggests that effective operation of DL(9) LIB can be carried out with initial 4.7 V UCV activation cycles, followed by 4.3 V UCV usage cycles.

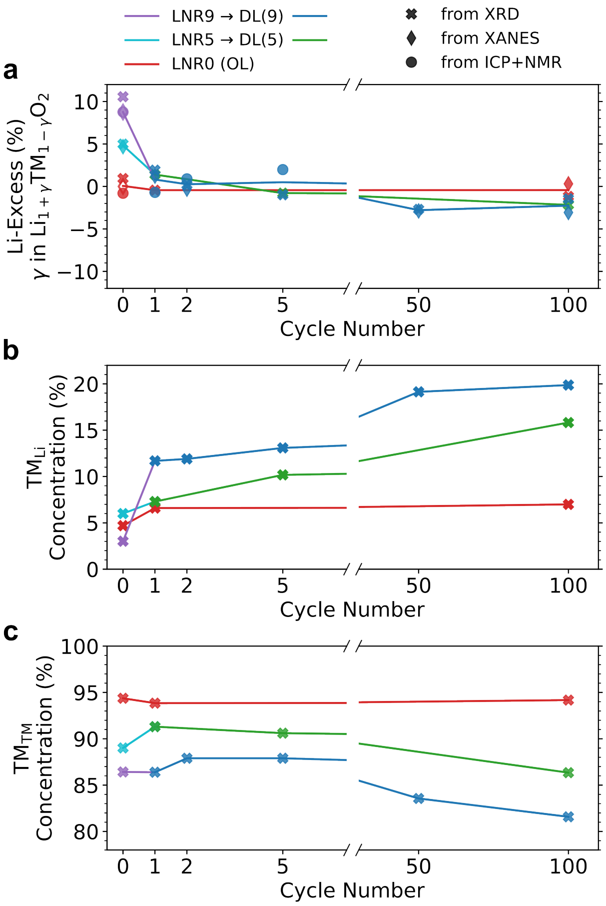

Supplementary Fig. 14 | **a**–**c**, Changes in composition (**a**) (determined by ICP+NMR, XRD, and XANES), TM_{Li} concentration (**b**) and TM_{TM} concentration (**c**) (determined by XRD) for as-synthesized LNR0, LNR5 and LNR9, as well as the activated DL(5) and DL(9), against the total number of electrochemical cycles (2.5–4.7 V). A condensed plot of these results is shown in Fig. 2a.

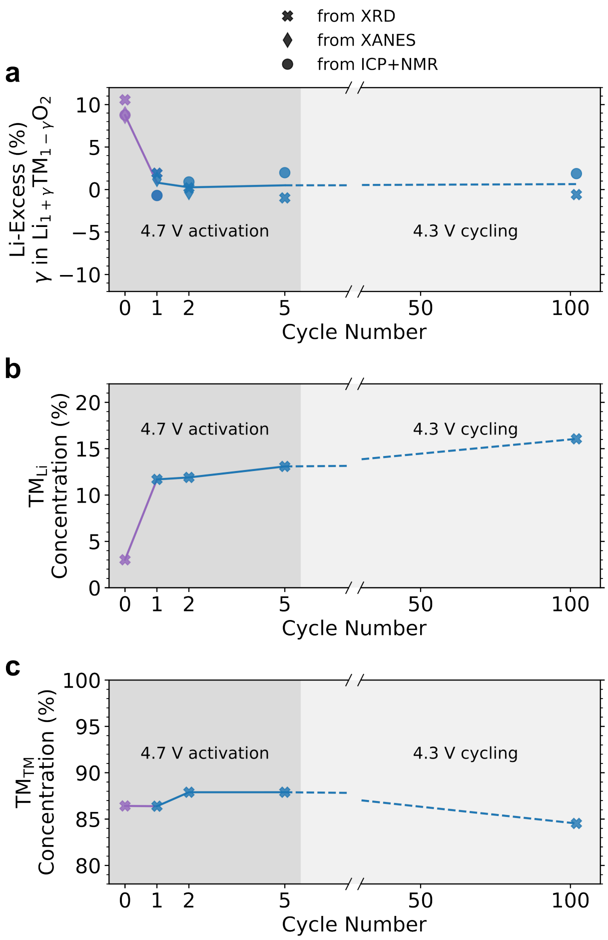

Supplementary Fig. 15 | **a**–**c**, Changes in composition (**a**), TM_{Li} concentration (**b**) and TM_{TM} concentration (**c**) for LNR9 and activated DL(9) determined by different techniques. The ≈100 cycled sample had a combination of 4.7 V UCV (5 cycles) and 4.3 V UCV (the rest), while the other samples only had 4.7 V UCV cycles. A condensed plot of these results is shown in Fig. 3c.

5. Supplementary Discussion: Lattice Parameter Evolution During Delithiation

5.1. Lattice parameter evolution during delithiation of OL, DL(5), and DL(9).

Supplementary Figs. 16–18 show the voltage profiles and XRD spectra for the delithiation of OL, DL(5), and DL(9). Based on Supplementary Fig. 14, DL(5) may require more cycles to plateau $\mathrm{TM_{Li}}$. Therefore, *operando* XRD for DL(5) was conducted on its 5^{th} charge (6^{th} if counting from LNR5) to ensure structural activation has completed beforehand. In Supplementary Fig. 19, lattice parameters, unit cell volume, and quantities related to strain anisotropy (**c**/**a** ratio and the difference between **c**- and **a**-strain) are plotted against remaining Li per formula unit (x_{Li}) of the electrochemically-active phase of cathode. It can be seen from Supplementary Fig. 19b that the trend in **a** (representing in-plane dimension) is very similar between OL and DL(9), with an almost linear decrease with Li content at large x_{Li}. This behavior matches closely with the theory presented in Supplementary Information section 2.2, which states that **a** is mostly influenced by the ionic radii and hence oxidation state of TM ions. The similarity in the behaviors of **a** testifies that the redox mechanism is similar between OL and DL, being almost entirely Ni-redox. The trend in **c** (Supplementary Fig. 19a) is very different between the samples, which we show to be $\mathrm{TM_{Li}}$-dependent and is discussed in more depth in the main article. The inhibition of **c**-collapse in DL(9) also suppressed its volume shrinkage (Supplementary Fig. 19c).

Besides dimensional changes, anisotropic strain during cathode cycling is another critical factor causing particle cracking[88]. Supplementary Fig. 19d,e shows two parameters often used to represent anisotropic strain. During charging of OL, the decrease of **a** coupled with increase of **c** resulted in particle shape stretching along the **c**-direction at low SOC. Whereas at high SOC, **c**-collapse resulted in a sudden change to shape compression along **c**. It is obvious that strain anisotropy was limited to a very small extent due to the almost invariant **c** in DL(9).

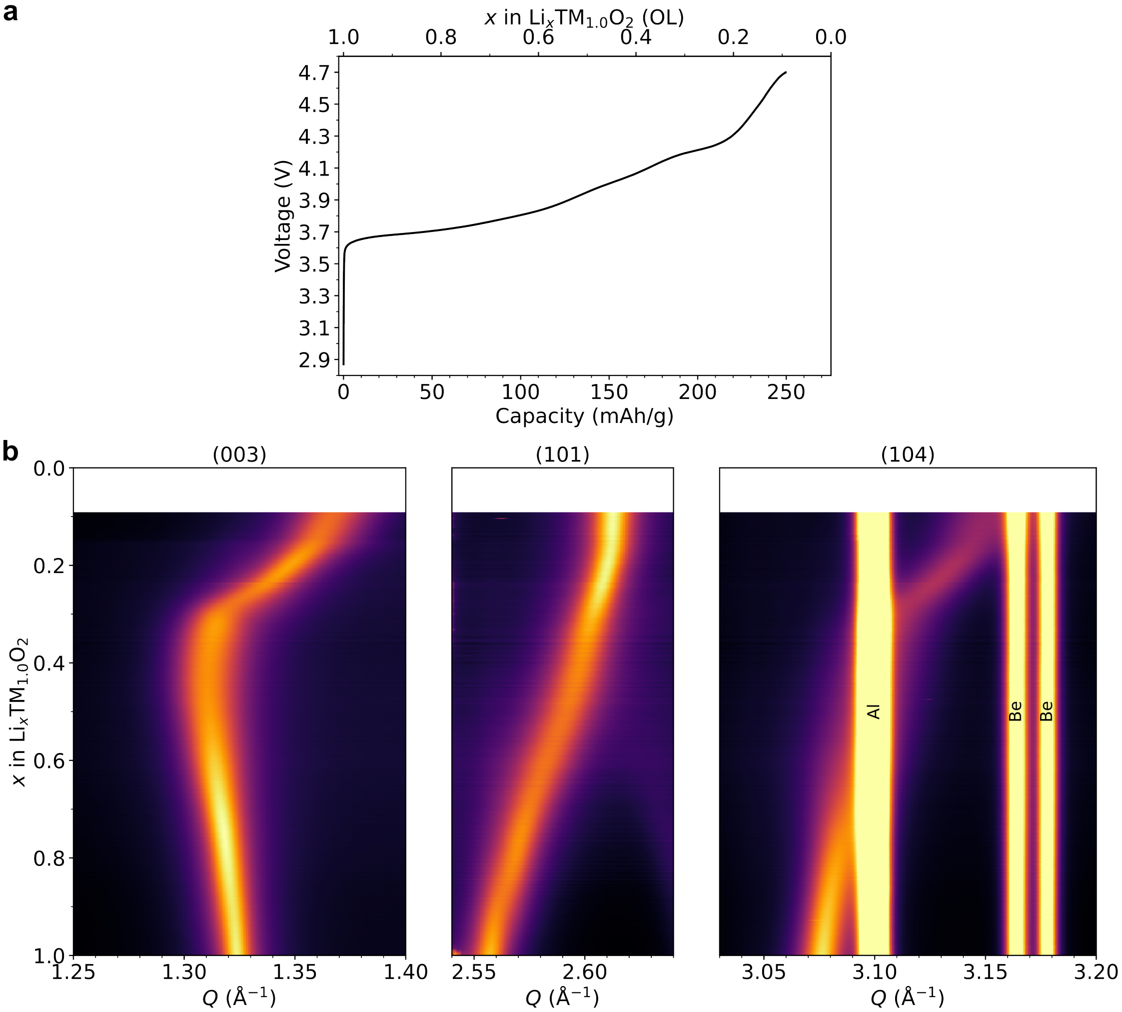

Supplementary Fig. 16 | **a**,**b**, Voltage profile (**a**) and evolution of (003), (101), and (104) diffraction peaks (**b**) during the 1st charge of OL (LNR0) from *operando* XRD measurement. X-ray wavelength: 0.97625 Å.

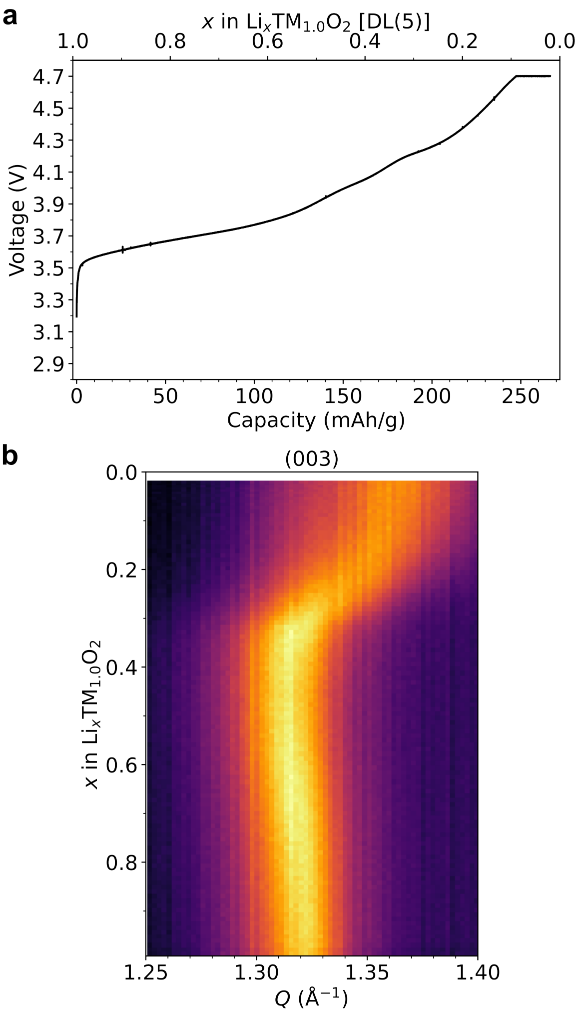

Supplementary Fig. 17 | a,**b**, Voltage profile (**a**) and evolution of (003) diffraction peak (**b**) during charging of DL(5) (6th charge of LNR5) from *operando* XRD measurement. Specific capacity is based on the estimated CAM mass in the harvested DL(5) electrode prior to *operando* cell assembly. X-ray source: Mo K_α.

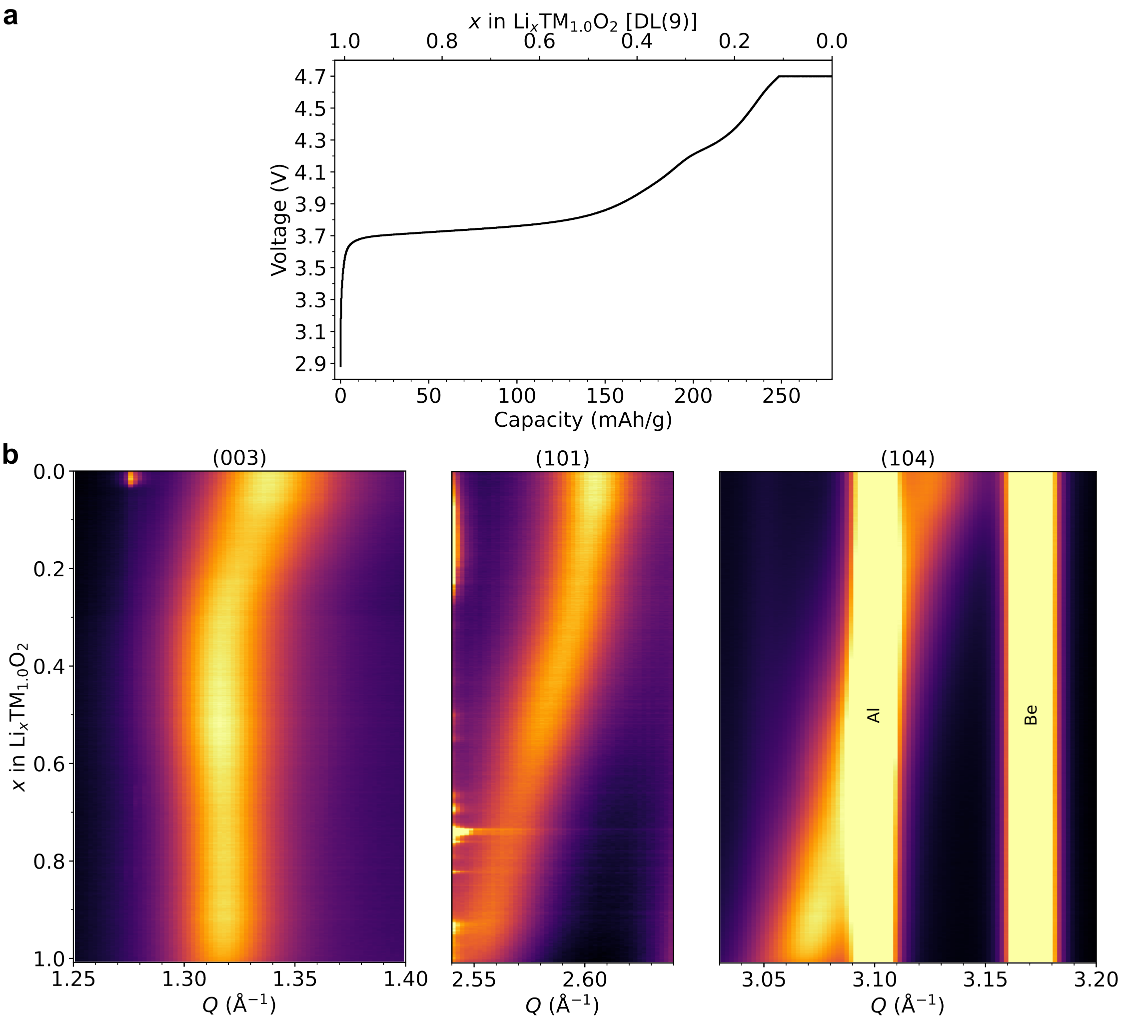

Supplementary Fig. 18 | a,**b**, Voltage profile (**a**) and evolution of (003), (101), and (104) diffraction peaks (**b**) during charging of DL(9) (2nd charge of LNR9) from *operando* XRD measurement. Specific capacity is based on the estimated CAM mass in the harvested DL(9) electrode prior to *operando* cell assembly. X-ray wavelength: 0.24058 Å.

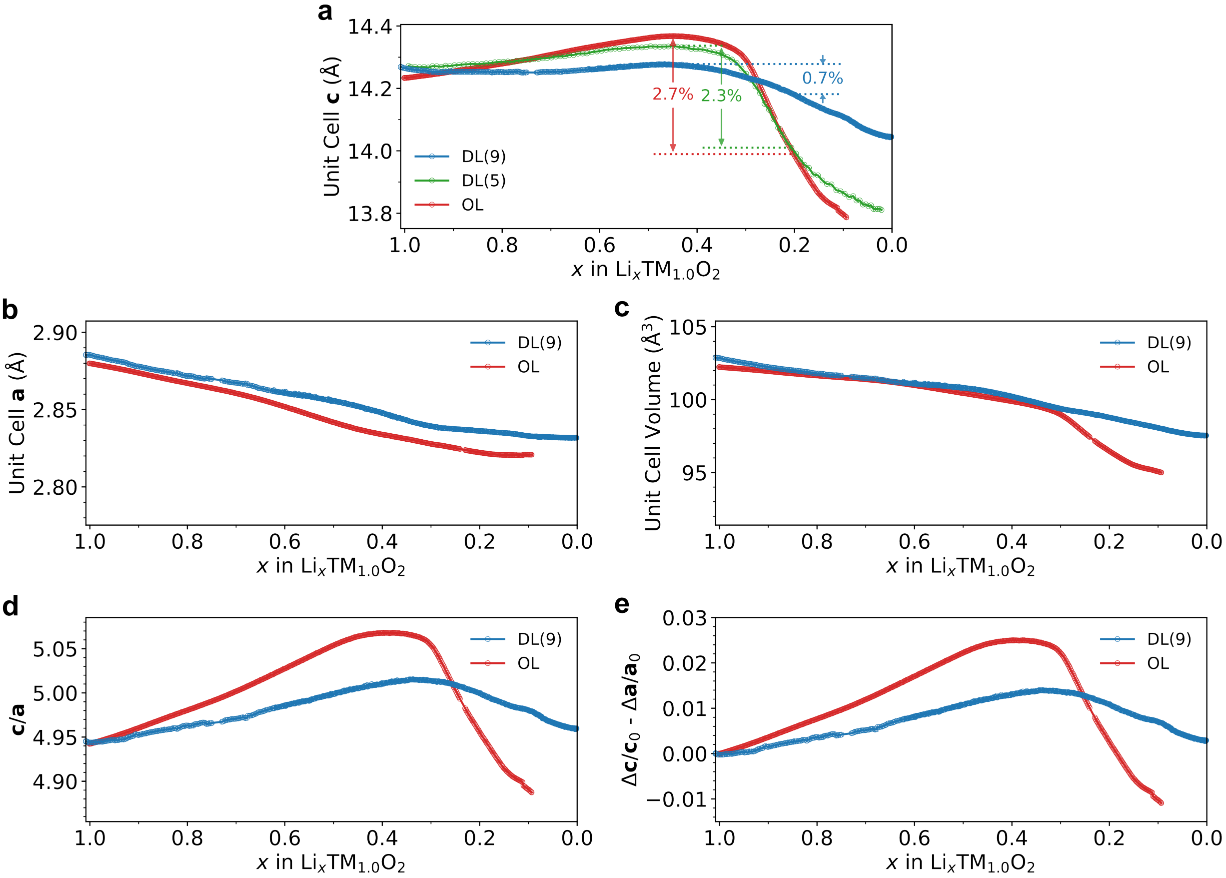

Supplementary Fig. 19 | **a**, Changes in **c** lattice parameter for OL, activated DL(5) and DL(9) upon delithiation. The percentages of **c**-collapse from maximum to 80% delithiation are highlighted. This is a duplicate of Fig. 2c. **b**–**e**, Changes in **a** lattice parameter (**b**), unit cell volume (**c**), lattice **c**/**a** ratio (**d**), and strain differential between the **c**- and **a**-directions (**e**) upon delithiation for OL and activated DL(9) determined from *operando* XRD. DL(9): 1st charge (*i.e.*, LNR9 – 2nd charge). DL(5): 5th charge (*i.e.*, LNR5 – 6th charge). OL (*i.e.* LNR0): 1st charge.

In Supplementary Fig. 20, the same measurement results are plotted against voltage. With CC 4.3 V cut-off as the baseline for comparison, **c**-strain maximum was 2.6% for OL, 1.6% for DL(5), and 0.6% for DL(9).

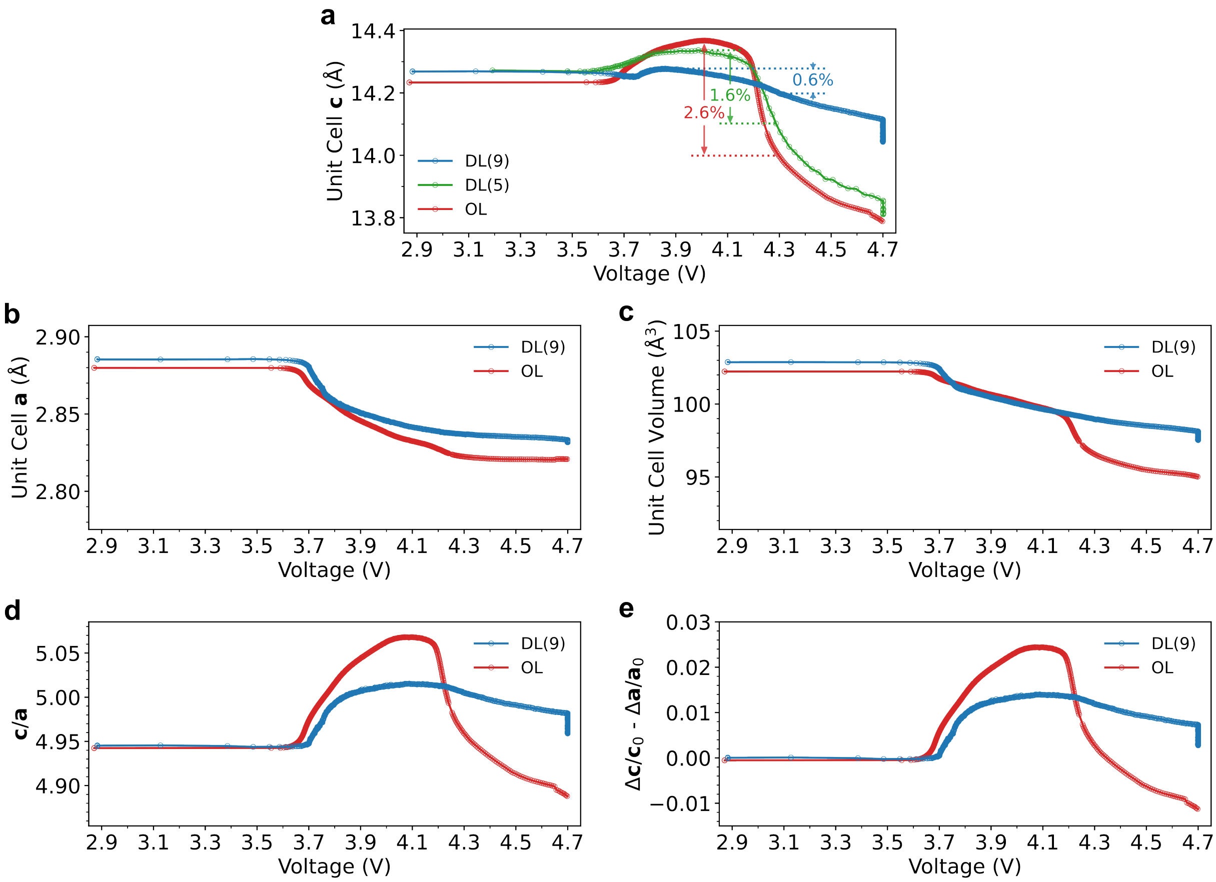

Supplementary Fig. 20 | **a**, Changes in **c** lattice parameter for OL, activated DL(5) and DL(9) upon charging. The percentages of **c**-collapse from maximum to 4.3 V are highlighted. **b**–**e**, Changes in **a** lattice parameter (**b**), unit cell volume (**c**), lattice **c**/**a** ratio (**d**), and strain differential between the **c**- and **a**-directions (**e**) against voltage (*vs.* Li/Li^+) for OL and activated DL(9) determined from *operando* XRD. DL(9): 1st charge (*i.e.*, LNR9 – 2nd charge). DL(5): 5th charge (*i.e.*, LNR5 – 6th charge). OL (*i.e.* LNR0): 1st charge.

5.2. Lattice parameter evolution during delithiation of aged DL(9).

Supplementary Fig. 21 shows the voltage profile and XRD spectra for the 100th 2.5–4.7 V cycle of DL(9). Supplementary Fig. 22 further compares the lattice parameters and strain anisotropy between the 1st and 100th charge of DL(9). It can be seen that there is no difference in lattice parameters between the 1st and 100th charge of DL(9) when x_{Li} of the electrochemically-active phase of cathode is the same.

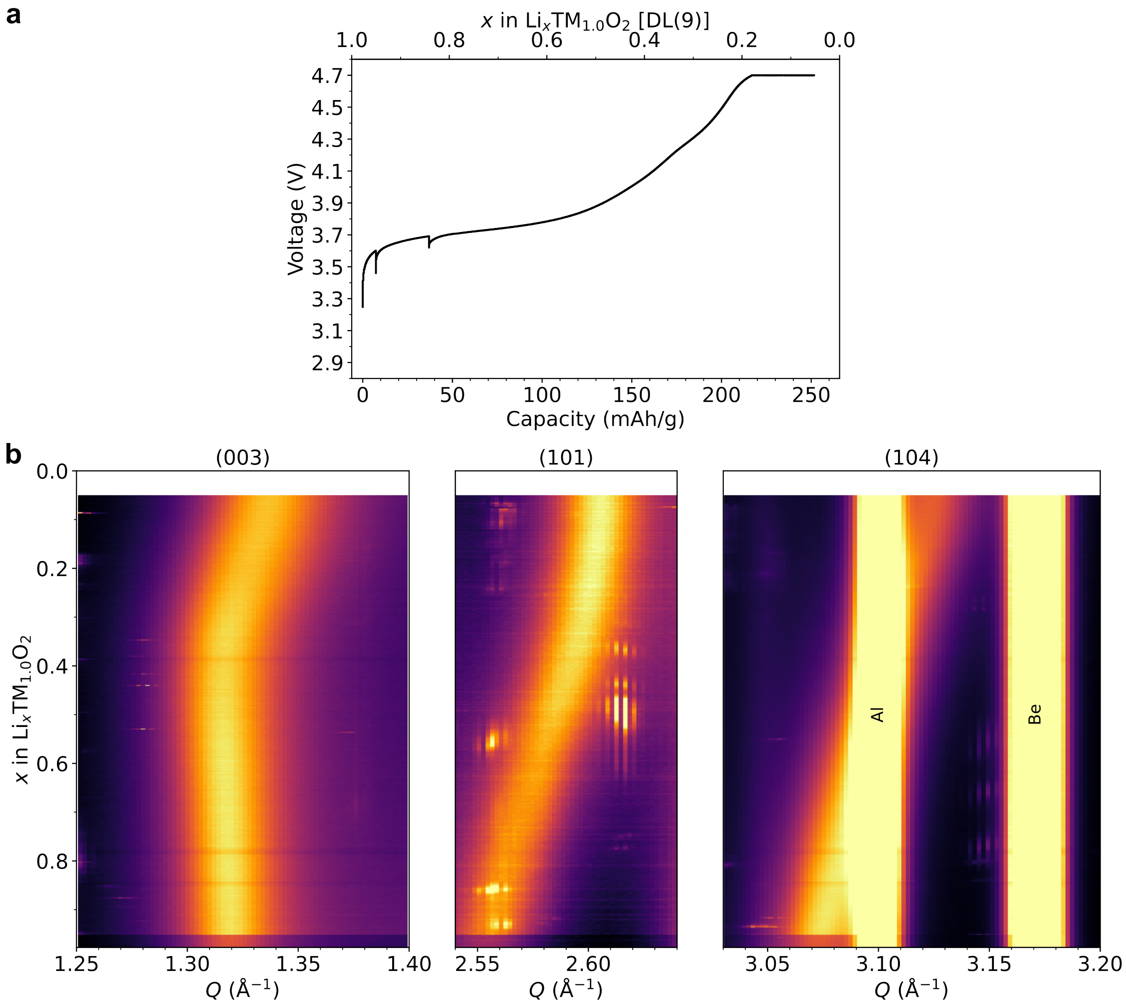

Supplementary Fig. 21 | **a**,**b**, Voltage profile (**a**) and evolution of (003), (101), and (104) diffraction peaks (**b**) during charging of aged DL(9) (101th charge of LNR9) from *operando* XRD measurement. Specific capacity is based on the estimated CAM mass in the harvested DL(9) electrode prior to *operando* cell assembly. The sample underwent 100 cycles of 2.5–4.7 V cycling prior to *operando* measurement. X-ray wavelength: 0.24058 Å.

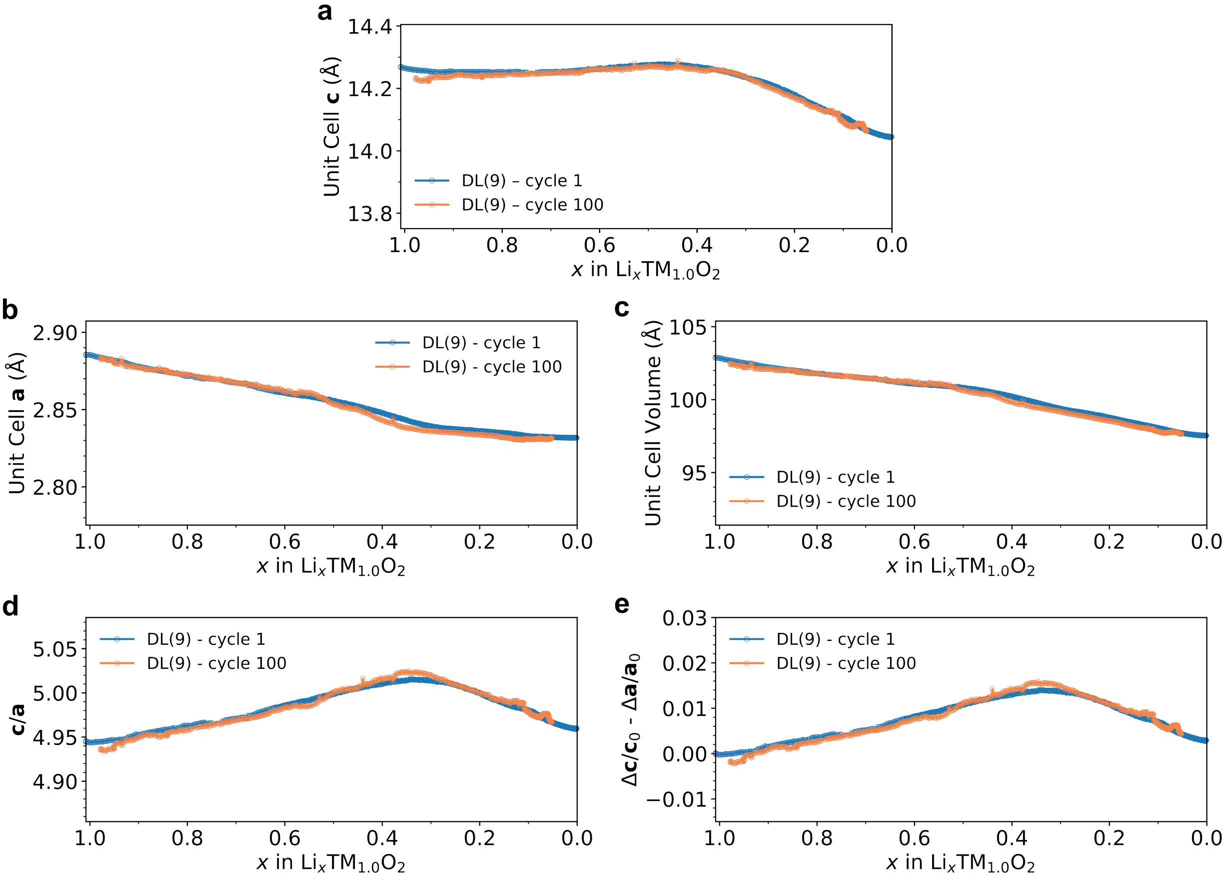

Supplementary Fig. 22 | **a**–**e**, Changes in **c** lattice parameter (**a**), **a** lattice parameter (**b**), unit cell volume (**c**), lattice **c**/**a** ratio (**d**), and strain differential between the **c**- and **a**-directions (**e**) upon delithiation for the 1st and 100th charge of DL(9) determined from *operando* XRD. Panel **a** is a duplicate of Fig. 3a.

In Supplementary Fig. 23, the same measurement results are plotted against voltage. It can be seen that although the lattice parameter values overlap when plotted against x_{Li}, there is a very small offset when plotted against voltage. This small offset is related to the build-up of polarization over extended cycling.

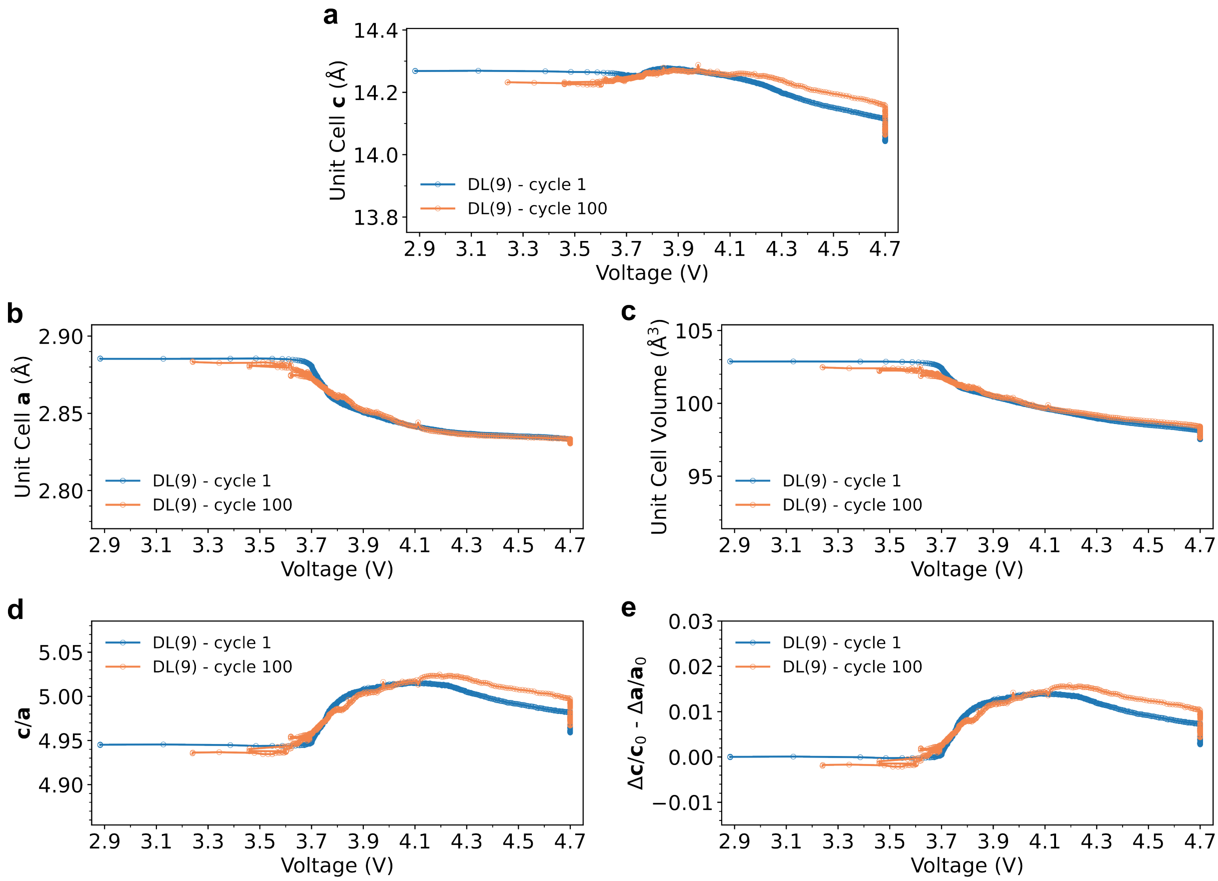

Supplementary Fig. 23 | **a**–**e**, Changes in **c** lattice parameter (**a**), **a** lattice parameter (**b**), unit cell volume (**c**), lattice **c**/**a** ratio (**d**), and strain differential between the **c**- and **a**-directions (**e**) against voltage (*vs.* Li/Li$^+$) for the 1st and 100th charge of DL(9) determined from *operando* XRD.

6. Supplementary Discussion: Electrochemical Evaluation

6.1. Capacity retention test with 2.5–4.3 V voltage window.

The behavior of DL(9) tested with the protocol of 5 initial 4.7 V UCV cycles followed by extended 4.3 V UCV usage cycles is discussed in the main article (Fig. 3b,d). Supplementary data to this test is presented in Supplementary Fig. 24, showing the voltage profiles, discharge capacities, and different types of mean voltages.

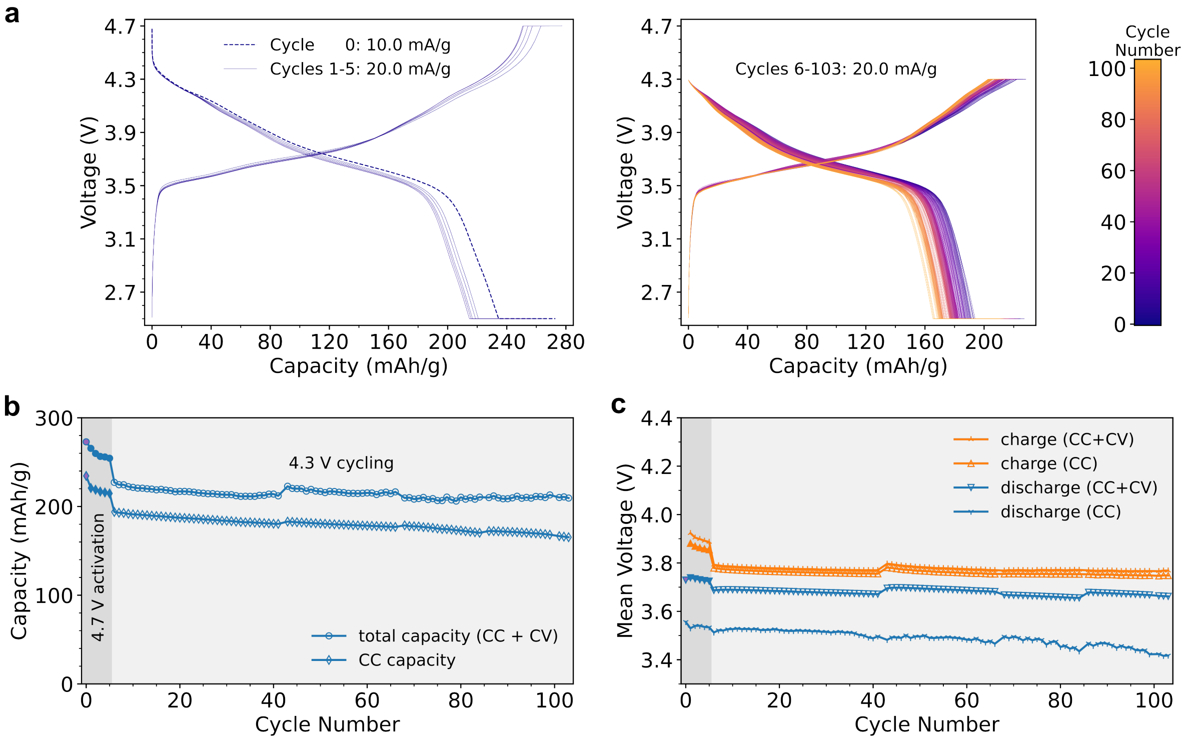

Supplementary Fig. 24 | Supplementary data on the capacity retention test of DL(9) using the cycling protocol of a few 4.7 UCV cycles followed by extended 4.3 V UCV usage cycles. Cycle 0 denotes first activation cycle that leads to the evolution of LNR9 to DL(9). **a**, Voltage profiles during the entire test. The charge profile of cycle 0 is excluded (because of the drastically different activation profile). The CC current used for each cycle is labeled. **b**, Change of discharge capacity with cycle number. **c**, Change of capacity-averaged voltage during charge and discharge. CC+CV quantities are calculated from the combined CC and CV segments of the test, whereas CC quantities are calculated based only on the CC segment. CV hold limit: 4 mA g^{-1} current for charge; 0.4 mA g^{-1} current for discharge. Test temperature: 30 ℃. Power outages impacted several cycles during the test, and the affected cycles are excluded from the plots.

Supplementary Fig. 25 presents the data of OL half-cell test using similar protocol (*i.e.*, extended 4.3 V UCV usage cycling). The only difference is that there is only one cycle with 4.7 V UCV since OL does not require high voltage activation, and an even slower current was used during CC segments.

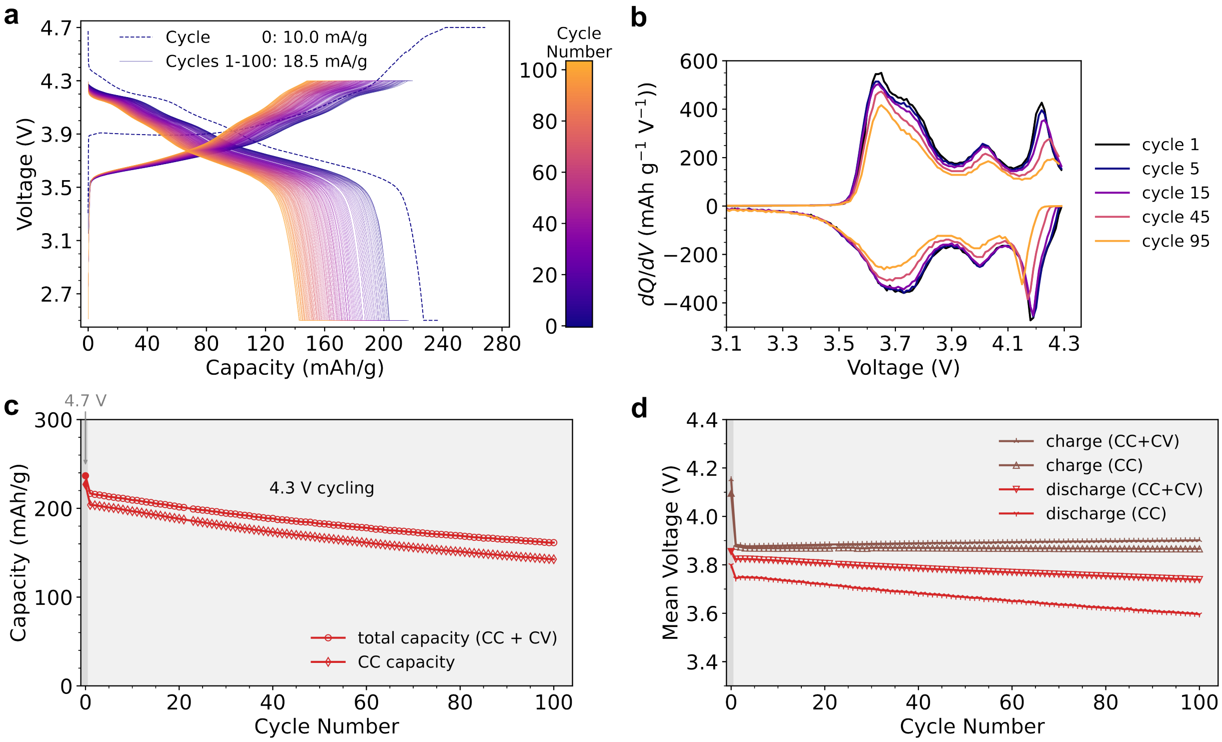

Supplementary Fig. 25 | Capacity retention test of OL with mostly 4.3 V UCV cycling. The first cycle with 4.7 V UCV cutoff is denoted as cycle 0. **a**, Voltage profiles during the entire test. The CC current used for each cycle is labeled. **b**, Differential capacity *vs.* voltage curves for selected cycles. **c**, Change of discharge capacity with cycle number. **d**, Change of capacity-averaged voltage during charge and discharge. CC+CV quantities are calculated from the combined CC and CV segments of the test, whereas CC quantities are calculated based only on the CC segment. CV hold limit: 4 mA g^{-1} current for charge; 0.4 mA g^{-1} current for discharge. Test temperature: 30 ℃. Power outages impacted several cycles during the test, and the affected cycles are excluded from the plots.

Supplementary Fig. 26 compares the capacity retention and voltage hysteresis between DL(9) and OL within the 4.3 V UCV usage cycles. It can be seen from Supplementary Fig. 26a,b that the initial discharge capacity is comparable between OL and DL(9). However, capacity retention is much better for DL(9) after 100 cycles, even if a higher rate was used during the test of DL(9) than OL (18.5 mA g^{-1} CC for OL *vs.* 20.0 mA g^{-1} CC for DL(9)). OL has initial total & CC discharge capacities of 216.8 and 203.8 mAh g^{-1}, respectively, with only 74.4% and 70.0% total & CC capacity retention after 100 cycles. This percentage of capacity retention is similar to the other Ni-rich cathodes reported in recent literature[7,89]. For DL(9), the initial total & CC discharge capacities are 227.2 and 193.9 mAh g^{-1}, respectively, and remarkably higher 92.2% and 85.3% total & CC capacity retention is delivered after 100 cycles.

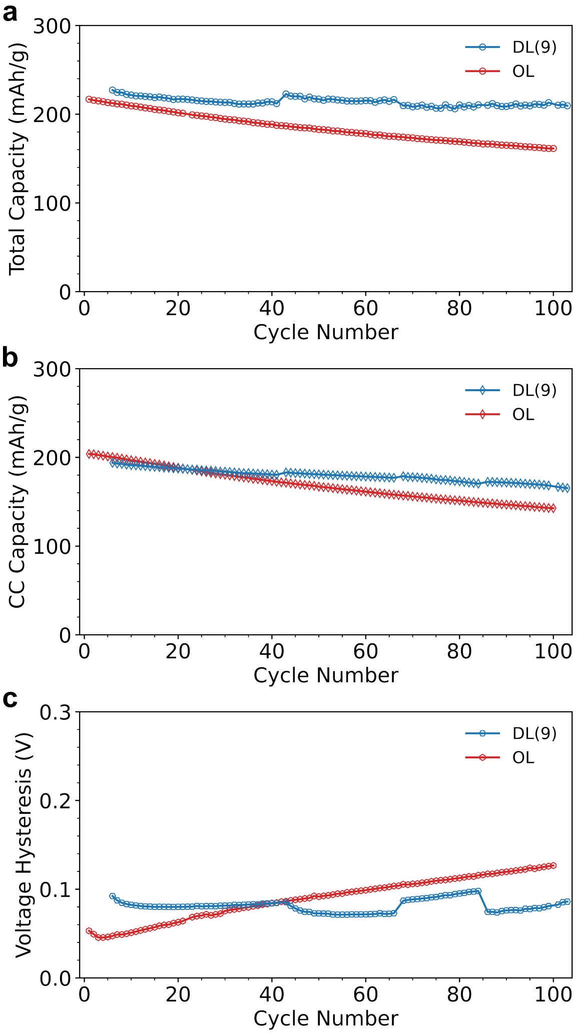

Supplementary Fig. 26 | **a**–**c**, Comparison between DL(9) and OL with the same 4.3 V UCV cycles, showing the change of total discharge capacity (**a**), CC discharge capacity (**b**), and CC voltage hysteresis (*i.e.* difference in mean CC voltage between charge and discharge) (**c**) with cycle number. OL was tested with a slightly slower rate: OL: 18.5 mA g^{-1} CC; DL(9): 20.0 mA g^{-1} CC. Power outages impacted several cycles during the test, and the affected cycles are excluded from the plots.

In addition, DL(9) displays more stable mean voltage and voltage hysteresis than OL (Supplementary Figs. 24c, 25d, and 26c). While the voltage hysteresis increased from 53 mV to 127 mV during the 100 cycles for OL, the voltage hysteresis remained relatively stable over 100 cycles for DL(9), averaging 81 mV hysteresis. From Supplementary Fig. 25b,d, it can be seen that changes in mean voltage for OL is mainly due to increased overpotentials. This is most obvious at the H2–H3 phase transition at around 4.2 V, where its associated dQ/dV peaks shift to higher potentials during charge and to lower potentials during discharge. In addition, decrease in the H2–H3 intensities with cycling are observed for OL. These changes to H2–H3 peak are commonly observed in Ni-rich cathodes and are likely manifestations of increased surface parasitic reactions due to microcrack formation and electrolyte penetration[7,90]. For DL(9), the M–H2 and H2–H3 transitions (Fig. 3d) are less abrupt from the start, which is probably a result of partial disorder in the crystal structure. Little change happens to both the potential and intensity of these dQ/dV peaks in DL(9) throughout the 100 cycles, suggesting high electrochemical stability at both the crystal structure and microstructure levels.

6.2. Rate capability test (2.5–4.7 V voltage window).

The discharge rate capability test result for DL(9) (2.5–4.7 V voltage window) is presented in Supplementary Fig. 27. As can be seen in Supplementary Fig. 27a, DL(9) attains 229.3 mAh g^{-1} initial C/20 capacity. When the discharge rate gradually increases, the average discharge capacity (over the two same-rate cycles) for DL(9) becomes 209.9 mAh g^{-1} at C/10, 162.3 mAh g^{-1} at C/2, 136.8 mAh g^{-1} at 1C, 87.0 mAh g^{-1} at 3C, and 69.1 mAh g^{-1} at 5C. When the discharge condition is reverted back to C/20 CC with CV hold at the end of the test, DL(9) attains 210.7 mAh g^{-1} CC capacity in the last test cycle. Referencing to its C/10 capacity (as 100%), its discharge capacity is 77%, 65%, and 41% at C/2, 1C, and 3C, respectively. Compared to typical well-ordered Ni-rich layered cathodes tested under similar conditions[91,92], DL(9) exhibits approximately 10–15% lower 1C rate performance, which is anticipated based on the expected decrease in Li diffusivity with disorder (Supplementary Information section 2.1). Despite this, it is important to note that the voltage profile for DL(9) has a similar shape regardless of discharge rate (Supplementary Fig. 27c), and therefore the impact of rate on average voltage is limited (Supplementary Fig. 27b). In this regard, the high-rate behavior of DL(9) is significantly better than other anion-redox cathodes known to have large voltage hysteresis, such as LMR.

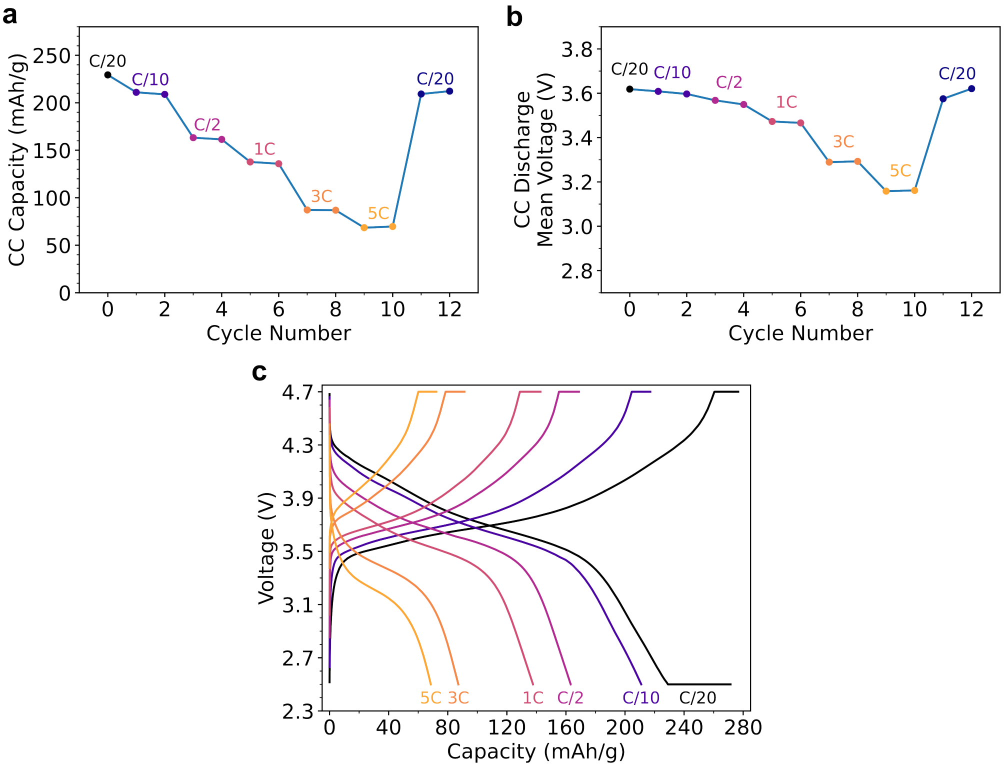

Supplementary Fig. 27 | Result of discharge rate performance test (4.7 V UCV) for DL(9). Cycle 0 denotes the first activation cycle that leads to the evolution of LNR9 to DL(9). **a**,**b**, CC discharge capacity (**a**), and CC discharge capacity-averaged voltage (**b**) obtained during rate test. **c**, Selected voltage profiles. For each discharge rate, the first discharge half-cycle and the subsequent charge half-cycle are plotted. 1C is defined as 200 mA g^{-1} current. All charge half-cycles used 20 mA g^{-1} CC followed by CV hold until 4 mA g^{-1} to ensure the cathode is similarly delithiated prior to discharge. For discharge, C/20 half-cycles had CV hold until 0.4 mA g^{-1}. All other discharge half-cycles had no CV hold. Test temperature: 30 ℃.

The rate performance of LMR ($Li_{1.34}(Mn_{0.34}Ni_{0.66})_{0.66}O_2$) is evaluated to demonstrate the differences (Supplementary Fig. 28). LMR is a promising family of high-capacity cathodes attracting significant interest in recent years[18,35,36]. Oxygen redox is utilized in LMR to boost its capacity. However, it suffers from voltage hysteresis, poor rate performance, and voltage decay over cycling. As can been seen in Supplementary Fig. 28a, with a 2.5–4.7 V voltage window, LMR attained 218.4 mAh g^{-1} initial C/20 capacity. When the discharge rate gradually increases, the average discharge capacity (over the two same-rate cycles) for LMR becomes 203.0 mAh g^{-1} at C/10, 188.1 mAh g^{-1} at C/5, 139.3 mAh g^{-1} at 1C, 76.5 mAh g^{-1} at 3C, and 36.8 mAh g^{-1} at 5C. When the discharge condition is reverted back to C/20 CC at the end of the test, LMR attains 216.7 mAh g^{-1} capacity in the last test cycle. In terms of relative capacity, the rate performance of LMR is similar to DL(9): 67% at 1C, and 38% at 3C (with 100% referenced to C/10 capacity). However, the voltage behavior of LMR is significantly worse than DL(9). Severe distortions to the shape of voltage profile can be seen for LMR at high C-rates (Supplementary Fig. 28c). This leads to a dramatic reduction in average voltage (Supplementary Fig. 28b) and therefore very low discharge energy of LMR at high rates.

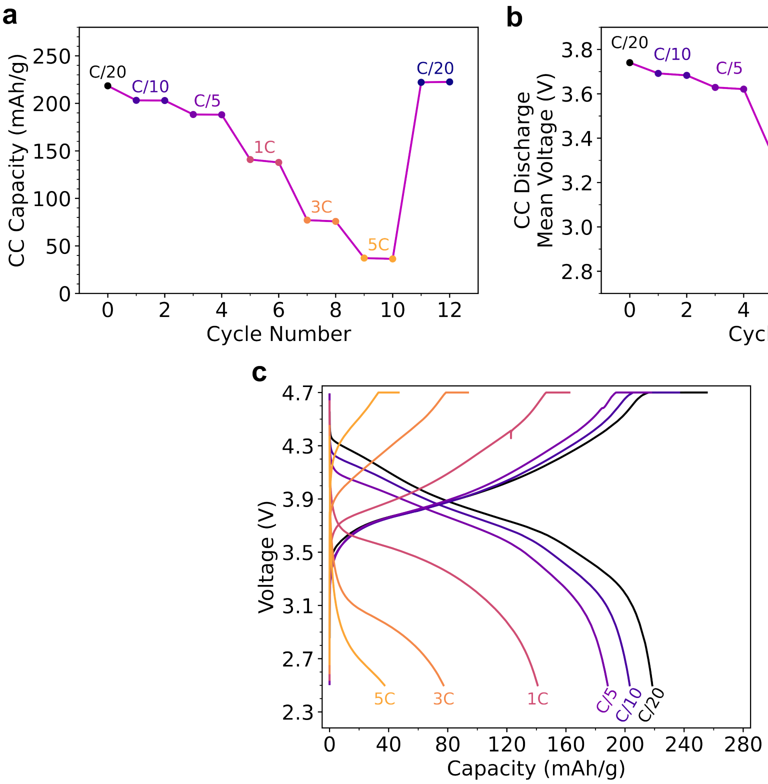

Supplementary Fig. 28 | Result of discharge rate performance test (4.7 V UCV) for LMR. Cycle 0 is the first cycle. **a**,**b**, CC discharge capacity (**a**), and CC discharge capacity-averaged voltage (**b**) obtained during rate test. **c**, Selected voltage profiles. For each discharge rate, the first discharge half-cycle and the subsequent charge half-cycle are plotted. 1C is defined as 200 mA g^{-1} current. All charge half-cycles used 20 mA g^{-1} CC followed by CV hold until 4 mA g^{-1} to ensure the cathode is fully delithiated prior to discharge. All discharge half-cycles had no CV hold. Test temperature: 30 ℃.

1. Goodenough, J. B. & Park, K.-S. The Li-Ion Rechargeable Battery: A Perspective. *J. Am. Chem. Soc.* **135**, 1167–1176 (2013).
2. Li, W., Asl, H. Y., Xie, Q. & Manthiram, A. Collapse of $LiNi_{1-x-y}Co_xMn_yO_2$ Lattice at Deep Charge Irrespective of Nickel Content in Lithium-Ion Batteries. *J. Am. Chem. Soc.* **141**, 5097–5101 (2019).
3. Kondrakov, A. O. *et al.* Charge-Transfer-Induced Lattice Collapse in Ni-Rich NCM Cathode Materials during Delithiation. *J. Phys. Chem. C* **121**, 24381–24388 (2017).
4. Lee, W. *et al.* New Insight into Ni-Rich Layered Structure for Next-Generation Li Rechargeable Batteries. *Adv. Energy Mater.* **8**, 1701788 (2018).
5. Bianchini, M., Roca-Ayats, M., Hartmann, P., Brezesinski, T. & Janek, J. There and Back Again—The Journey of $LiNiO_2$ as a Cathode Active Material. *Angew. Chemie Int. Ed.* **58**, 10434–10458 (2019).
6. Lee, S., Su, L., Mesnier, A., Cui, Z. & Manthiram, A. Cracking vs. surface reactivity in high-nickel cathodes for lithium-ion batteries. *Joule* **7**, 2430–2444 (2023).
7. Ryu, H.-H., Park, K.-J., Yoon, C. S. & Sun, Y.-K. Capacity Fading of Ni-Rich $Li[Ni_xCo_yMn_{1-x-y}]O_2$ ($0.6 \leq x \leq 0.95$) Cathodes for High-Energy-Density Lithium-Ion Batteries: Bulk or Surface Degradation? *Chem. Mater.* **30**, 1155–1163 (2018).
8. Xie, Q., Li, W. & Manthiram, A. A Mg-Doped High-Nickel Layered Oxide Cathode Enabling Safer, High-Energy-Density Li-Ion Batteries. *Chem. Mater.* **31**, 938–946 (2019).
9. Wang, L., Liu, T., Wu, T. & Lu, J. Strain-retardant coherent perovskite phase stabilized Ni-rich cathode. *Nature* **611**, 61–67 (2022).
10. Li, N. *et al.* Layered-rocksalt intergrown cathode for high-capacity zero-strain battery operation. *Nat. Commun.* **12**, 2348 (2021).
11. Li, B. *et al.* Constructing "Li-rich Ni-rich" oxide cathodes for high-energy-density Li-ion batteries. *Energy Environ. Sci.* **16**, 1210–1222 (2023).
12. Zhang, R. *et al.* Compositionally complex doping for zero-strain zero-cobalt layered cathodes. *Nature* **610**, 67–73 (2022).
13. Yin, L. *et al.* Thermodynamics of Antisite Defects in Layered NMC Cathodes: Systematic Insights from High-Precision Powder Diffraction Analyses. *Chem. Mater.* **32**, 1002–1010 (2020).
14. Hua, W. *et al.* Long-Range Cationic Disordering Induces two Distinct Degradation Pathways in Co-Free Ni-Rich Layered Cathodes. *Angew. Chemie Int. Ed.* **62**, e202214880 (2023).
15. Duan, Y. *et al.* Insights into Li/Ni ordering and surface reconstruction during synthesis of Ni-rich layered oxides. *J. Mater. Chem. A* **7**, 513–519 (2019).
16. Wagner, A. C. *et al.* Hierarchical Structuring of NMC111-Cathode Materials in Lithium-Ion Batteries: An In-Depth Study on the Influence of Primary and Secondary Particle Sizes on Electrochemical Performance. *ACS Appl. Energy Mater.* **3**, 12565–12574 (2020).
17. Assat, G. & Tarascon, J.-M. Fundamental understanding and practical challenges of anionic redox activity in Li-ion batteries. *Nat. Energy* **3**, 373–386 (2018).
18. Gent, W. E. *et al.* Coupling between oxygen redox and cation migration explains unusual electrochemistry in lithium-rich layered oxides. *Nat. Commun.* **8**, 2091 (2017).
19. Eum, D. *et al.* Voltage decay and redox asymmetry mitigation by reversible cation migration in lithium-rich layered oxide electrodes. *Nat. Mater.* **19**, 419–427 (2020).
20. Yin, W. *et al.* Structural evolution at the oxidative and reductive limits in the first electrochemical cycle of $Li_{1.2}Ni_{0.13}Mn_{0.54}Co_{0.13}O_2$. *Nat. Commun.* **11**, 1252 (2020).
21. Huang, J. *et al.* Inhibiting collective cation migration in Li-rich cathode materials as a strategy to mitigate voltage hysteresis. *Nat. Mater.* **22**, 353–361 (2023).
22. Bianchini, M. *et al.* From $LiNiO_2$ to Li_2NiO_3: Synthesis, Structures and Electrochemical Mechanisms in Li-Rich Nickel Oxides. *Chem. Mater.* **32**, 9211–9227 (2020).
23. Ying, J., Wan, C. & Jiang, C. Surface treatment of $LiNi_{0.8}Co_{0.2}O_2$ cathode material for lithium secondary batteries. *J. Power Sources* **102**, 162–166 (2001).
24. Park, K. *et al.* Improved Cycling Stability of $Li[Ni_{0.90}Co_{0.05}Mn_{0.05}]O_2$ Through Microstructure Modification by Boron Doping for Li-Ion Batteries. *Adv. Energy Mater.* **8**, 1801202 (2018).
25. Lin, J. & Fang, L. An Effective Way of Improving the Performance of Ni-Rich $LiNi_{0.82}Co_{0.12}Mn_{0.06}O_2$ Cathode in Lithium-Ion Battery via Borate Coating. *Energy Technol.* **9**, 2000721 (2021).
26. Su, Y. *et al.* Enhanced Electrochemical Performance of Ni-Rich Cathode Materials with an In Situ-Formed $LiBO_2/B_2O_3$ Hybrid Coating Layer. *ACS Appl. Energy Mater.* **5**, 2231–2241 (2022).
27. Xu, J. *et al.* Elucidating anionic oxygen activity in lithium-rich layered oxides. *Nat. Commun.* **9**, 947 (2018).
28. House, R. A. *et al.* First-cycle voltage hysteresis in Li-rich 3*d* cathodes associated with molecular O_2 trapped in the bulk. *Nat. Energy* **5**, 777–785 (2020).
29. Yan, P. *et al.* Injection of oxygen vacancies in the bulk lattice of layered cathodes. *Nat. Nanotechnol.* **14**, 602–608 (2019).
30. Grenier, A. *et al.* Nanostructure Transformation as a Signature of Oxygen Redox in Li-Rich 3d and 4d Cathodes. *J. Am. Chem. Soc.* **143**, 5763–5770 (2021).
31. Marie, J.-J. *et al.* Trapped O_2 and the origin of voltage fade in layered Li-rich cathodes. *Nat. Mater.* **23**, 818–825 (2024).
32. Hatsukade, T., Schiele, A., Hartmann, P., Brezesinski, T. & Janek, J. Origin of Carbon Dioxide Evolved during Cycling of Nickel-Rich Layered NCM Cathodes. *ACS Appl. Mater. Interfaces* **10**, 38892–38899 (2018).
33. Jung, R., Strobl, P., Maglia, F., Stinner, C. & Gasteiger, H. A. Temperature Dependence of Oxygen Release from $LiNi_{0.6}Mn_{0.2}Co_{0.2}O_2$ (NMC622) Cathode Materials for Li-Ion Batteries. *J. Electrochem. Soc.* **165**, A2869–A2879 (2018).
34. Wandt, J., Freiberg, A. T., Ogrodnik, A. & Gasteiger, H. A. Singlet oxygen evolution from layered transition metal oxide cathode materials and its implications for lithium-ion batteries. *Mater. Today* **21**, 825–833 (2018).
35. Csernica, P. M. *et al.* Persistent and partially mobile oxygen vacancies in Li-rich layered oxides. *Nat. Energy* **6**, 642–652 (2021).
36. Kim, S. Y. *et al.* Inhibiting Oxygen Release from Li-rich, Mn-rich Layered Oxides at the Surface with a Solution Processable Oxygen Scavenger Polymer. *Adv. Energy Mater.* **11**, 2100552 (2021).
37. McColl, K. *et al.* Transition metal migration and O_2 formation underpin voltage hysteresis in oxygen-redox disordered rocksalt cathodes. *Nat. Commun.* **13**, 5275 (2022).
38. Armstrong, A. R. *et al.* Demonstrating Oxygen Loss and Associated Structural Reorganization in the Lithium Battery Cathode $Li[Ni_{0.2}Li_{0.2}Mn_{0.6}]O_2$. *J. Am. Chem. Soc.* **128**, 8694–8698 (2006).
39. Wang, F. *et al.* Prelithiation: A Crucial Strategy for Boosting the Practical Application of Next-Generation Lithium Ion Battery. *ACS Nano* **15**, 2197–2218 (2021).
40. Shi, J. *et al.* Prelithiation of Lithium Peroxide for Silicon Anode: Achieving a High Activation Rate. *ACS Appl. Mater. Interfaces* **15**, 26710–26717 (2023).
41. Kim, Y., Kim, D. & Kang, S. Experimental and first-principles thermodynamic study of the formation and effects of vacancies in layered lithium nickel cobalt oxides. *Chem. Mater.* **23**, 5388–5397 (2011).
42. Zhang, M.-J. *et al.* Cationic Ordering Coupled to Reconstruction of Basic Building Units during Synthesis of High-Ni Layered Oxides. *J. Am. Chem. Soc.* **140**, 12484–12492 (2018).
43. Boulineau, A., Simonin, L., Colin, J.-F., Bourbon, C. & Patoux, S. First Evidence of Manganese–Nickel Segregation and Densification upon Cycling in Li-Rich Layered Oxides for Lithium Batteries. *Nano Lett.* **13**, 3857–3863 (2013).
44. Schomburg, F. *et al.* Lithium-ion battery cell formation: status and future directions towards a knowledge-based process design. *Energy Environ. Sci.* **17**, 2686–2733 (2024).
45. Kim, U. *et al.* Microstructure-Controlled Ni-Rich Cathode Material by Microscale Compositional Partition for Next-Generation Electric Vehicles. *Adv. Energy Mater.* **9**, 1803902 (2019).
46. Kim, U.-H. *et al.* Heuristic solution for achieving long-term cycle stability for Ni-rich layered cathodes at full depth of discharge. *Nat. Energy* **5**, 860–869 (2020).
47. de Biasi, L. *et al.* Phase Transformation Behavior and Stability of $LiNiO_2$ Cathode Material for Li-Ion Batteries Obtained from In Situ Gas Analysis and Operando X-Ray Diffraction. *ChemSusChem* **12**, 2240–2250 (2019).
48. Hu, J. *et al.* Extended fast-charging life of ultrahigh-Ni layered oxides by adjusting the current density during the $H2 \rightarrow H3$ phase transition. *Energy Storage Mater.* **50**, 751–759 (2022).
49. Clément, R. J., Lun, Z. & Ceder, G. Cation-disordered rocksalt transition metal oxides and oxyfluorides for high energy lithium-ion cathodes. *Energy Environ. Sci.* **13**, 345–373 (2020).
50. Massiot, D. *et al.* Modelling one- and two-dimensional solid-state NMR spectra. *Magn. Reson. Chem.* **40**, 70–76 (2002).
51. Park, J. *et al.* Fictitious phase separation in Li layered oxides driven by electro-autocatalysis. *Nat. Mater.* **20**, 991–999 (2021).
52. Ashiotis, G. *et al.* The fast azimuthal integration Python library: pyFAI. *J. Appl. Crystallogr.* **48**, 510–519 (2015).
53. Coelho, A. A. *TOPAS* and *TOPAS-Academic*: an optimization program integrating computer algebra and crystallographic objects written in C++. *J. Appl. Crystallogr.* **51**, 210–218 (2018).
54. Ravel, B. & Newville, M. *ATHENA*, *ARTEMIS*, *HEPHAESTUS*: data analysis for X-ray absorption spectroscopy using *IFEFFIT*. *J. Synchrotron Radiat.* **12**, 537–541 (2005).
55. Schindelin, J. *et al.* Fiji: an open-source platform for biological-image analysis. *Nat. Methods* **9**, 676–682 (2012).
56. Urban, A., Lee, J. & Ceder, G. The Configurational Space of Rocksalt-Type Oxides for High-Capacity Lithium Battery Electrodes. *Adv. Energy Mater.* **4**, 1400478 (2014).
57. Kang, K. & Ceder, G. Factors that affect Li mobility in layered lithium transition metal oxides. *Phys. Rev. B* **74**, 094105 (2006).
58. Lee, J. *et al.* Unlocking the Potential of Cation-Disordered Oxides for Rechargeable Lithium Batteries. *Science* **343**, 519–522 (2014).
59. Delmas, C., Fouassier, C. & Hagenmuller, P. Structural classification and properties of the layered oxides. *Phys. B+C* **99**, 81–85 (1980).
60. Bi, Y. *et al.* Reversible planar gliding and microcracking in a single-crystalline Ni-rich cathode. *Science* **370**, 1313–1317 (2020).
61. Tarascon, J. M. *et al.* *In Situ* Structural and Electrochemical Study of $Ni_{1x}Co_xO_2$ Metastable Oxides Prepared by Soft Chemistry. *J. Solid State Chem.* **147**, 410–420 (1999).
62. Müller, M., Schneider, L., Bohn, N., Binder, J. R. & Bauer, W. Effect of Nanostructured and Open-Porous Particle Morphology on Electrode Processing and Electrochemical Performance of Li-Ion Batteries. *ACS Appl. Energy Mater.* **4**, 1993–2003 (2021).
63. Park, K. *et al.* Elucidating and Mitigating High-Voltage Degradation Cascades in Cobalt-Free $LiNiO_2$ Lithium-Ion Battery Cathodes. *Adv. Mater.* **34**, 2106402 (2022).
64. Croguennec, L., Pouillerie, C., Mansour, A. N. & Delmas, C. Structural characterisation of the highly deintercalated $Li_xNi_{1.02}O_2$ phases (with $x \leq 0.30$). *J. Mater. Chem.* **11**, 131–141 (2001).
65. Wang, C. *et al.* Resolving complex intralayer transition motifs in high-Ni-content layered cathode materials for lithium-ion batteries. *Nat. Mater.* **22**, 235–241 (2023).
66. Luo, K. *et al.* Charge-compensation in 3*d*-transition-metal-oxide intercalation cathodes through the generation of localized electron holes on oxygen. *Nat. Chem.* **8**, 684–691 (2016).
67. Seo, D.-H. *et al.* The structural and chemical origin of the oxygen redox activity in layered and cation-disordered Li-excess cathode materials. *Nat. Chem.* **8**, 692–697 (2016).
68. House, R. A. *et al.* Delocalized electron holes on oxygen in a battery cathode. *Nat. Energy* **8**, 351–360 (2023).
69. Abate, I. I. *et al.* Coulombically-stabilized oxygen hole polarons enable fully reversible oxygen redox. *Energy Environ. Sci.* **14**, 4858–4867 (2021).
70. Kitchaev, D. A., Vinckeviciute, J. & Van der Ven, A. Delocalized Metal–Oxygen π-Redox Is the Origin of Anomalous Nonhysteretic Capacity in Li-Ion and Na-Ion Cathode Materials. *J. Am. Chem. Soc.* **143**, 1908–1916 (2021).
71. McCalla, E. *et al.* Visualization of O-O peroxo-like dimers in high-capacity layered oxides for Li-ion batteries. *Science* **350**, 1516–1521 (2015).
72. Ning, F. *et al.* Inhibition of oxygen dimerization by local symmetry tuning in Li-rich layered oxides for improved stability. *Nat. Commun.* **11**, 4973 (2020).
73. House, R. A. *et al.* The role of O_2 in O-redox cathodes for Li-ion batteries. *Nat. Energy* **6**, 781–789 (2021).
74. Gent, W. E., Abate, I. I., Yang, W., Nazar, L. F. & Chueh, W. C. Design Rules for High-Valent Redox in Intercalation Electrodes. *Joule* **4**, 1369–1397 (2020).
75. Assat, G. *et al.* Fundamental interplay between anionic/cationic redox governing the kinetics and thermodynamics of lithium-rich cathodes. *Nat. Commun.* **8**, 2219 (2017).
76. Bisogni, V. *et al.* Ground-state oxygen holes and the metal–insulator transition in the negative charge-transfer rare-earth nickelates. *Nat. Commun.* **7**, 13017 (2016).
77. Genreith-Schriever, A. R. *et al.* Oxygen hole formation controls stability in $LiNiO_2$ cathodes. *Joule* **7**, 1623–1640 (2023).
78. Aydinol, M. K., Kohan, A. F., Ceder, G., Cho, K. & Joannopoulos, J. *Ab initio* study of lithium intercalation in metal oxides and metal dichalcogenides. *Phys. Rev. B* **56**, 1354–1365 (1997).

79. Bianchini, M., Fauth, F., Hartmann, P., Brezesinski, T. & Janek, J. An *in situ* structural study on the synthesis and decomposition of $LiNiO_2$. *J. Mater. Chem. A* **8**, 1808–1820 (2020).
80. Dong, Y. & Li, J. Oxide Cathodes: Functions, Instabilities, Self Healing, and Degradation Mitigations. *Chem. Rev.* **123**, 811–833 (2023).
81. Hong, J. *et al.* Metal–oxygen decoordination stabilizes anion redox in Li-rich oxides. *Nat. Mat.* **18**, 2056 (2019).
82. Wang, W. *et al.* Stabilization of a 4.7 V High-Voltage Nickel-Rich Layered Oxide Cathode for Lithium-Ion Batteries through Boron-Based Surface Residual Lithium-Tuned Interface Modification Engineering. *ChemElectroChem* **8**, 2014–2021 (2021).
83. Chien, P. *et al.* New Insights into Structural Evolution of $LiNiO_2$ Revealed by Operando Neutron Diffraction. *Batter. Supercaps* **4**, 1701–1707 (2021).
84. Jung, R., Metzger, M., Maglia, F., Stinner, C. & Gasteiger, H. A. Oxygen Release and Its Effect on the Cycling Stability of $LiNi_xMn_yCo_zO_2$ (NMC) Cathode Materials for Li-Ion Batteries. *J. Electrochem. Soc.* **164**, A1361–A1377 (2017).
85. Li, S. *et al.* Anionic redox reaction and structural evolution of Ni-rich layered oxide cathode material. *Nano Energy* **98**, 107335 (2022).
86. Noh, H. J., Youn, S., Yoon, C. S. & Sun, Y. K. Comparison of the structural and electrochemical properties of layered $Li[Ni_xCo_yMn_z]O_2$ (x = 1/3, 0.5, 0.6, 0.7, 0.8 and 0.85) cathode material for lithium-ion batteries. *J. Power Sources* **233**, 121–130 (2013).
87. Yoon, C. S. *et al.* Cation Ordering of Zr-Doped $LiNiO_2$ Cathode for Lithium-Ion Batteries. *Chem. Mater.* **30**, 1808–1814 (2018).
88. Stallard, J. C. *et al.* Mechanical properties of cathode materials for lithium-ion batteries. *Joule* **6**, 984–1007 (2022).
89. Jun, D.-W., Yoon, C. S., Kim, U.-H. & Sun, Y.-K. High-Energy Density Core–Shell Structured $Li[Ni_{0.95}Co_{0.025}Mn_{0.025}]O_2$ Cathode for Lithium-Ion Batteries. *Chem. Mater.* **29**, 5048–5052 (2017).
90. Jamil, S. *et al.* Suppressing H2–H3 phase transition in high Ni–low Co layered oxide cathode material by dual modification. *J. Mater. Chem. A* **8**, 21306–21316 (2020).
91. Xue, W. *et al.* Ultra-high-voltage Ni-rich layered cathodes in practical Li metal batteries enabled by a sulfonamide-based electrolyte. *Nat. Energy* **6**, 495–505 (2021).
92. Wang, Y. *et al.* Surface modification enabling 4.7 V Nickel-rich layered cathode with superior long-term cyclability via novel functional polyimide binders. *J. Power Sources* **545**, 231927 (2022).